People's Democratic Republic of Algeria
Ministry of Higher Education and Scientific Research
Kasdi Merbah University - Ouargla

Faculty of Mathematics and Matter Sciences
Department of Physics

Doctoral Thesis

Field: Matter Sciences

Domain: Physics

Specialization: Radiation and Matter Physics

Presented by: Ahlam AOUACHIR

Title

Study of some Physical Properties of 1D-Photonic Crystals: Biosensing Applications

Publicly defended on 19/05/2026, before the examining committee:

Mr.	Abderrahim ACHOURI	Professeur	(University of Ouargla)	Chairman
Mr.	Khalfallah BENBELGACEM	MCA	(University of Ouargla)	Supervisor
Mr.	Kamal Eddine AIADI	Professeur	(University of Ouargla)	co-Supervisor
Mr.	Omar BENTOUILA	Professeur	(University of Ouargla)	Examiner
Mr.	Lazhar BENMEBROUK	Professeur	(University of Ouargla)	Examiner
Mr.	Mebrouk GHOUGALI	MCA	(University of Eloued)	Examiner
Mr.	Farhat RAHOUMA	Professeur	(University of Eloued)	Examiner

Academic Year 2025/2026

Dedication

To my dear parents,
in gratitude for their sacrifices, patience, and unwavering support, which formed the foundation of my academic journey.

To my beloved sister,
and to my dear brothers Ali , Djamal, and Hamza,
and to all members of my dear family,
thank you for your constant support and sincere encouragement.

To my professors and teachers,
in appreciation of their guidance, dedication, and valuable knowledge that shaped my academic and scientific path.

To my dear friends
H. Bouchellig, W. Chaib, I. Achouri, A. Aiadi, R. Hadjadj ,
in appreciation of their support, sincere friendship, and standing by my side throughout this journey.

This work is dedicated with sincere gratitude and respect.

Acknowledgements

All praise and thanks are due to Allah Almighty, for His guidance and blessings.
May peace and blessings be upon Prophet Muhammad.

The present work was conducted at the Laboratory for LENREZA, within the Optoelectronics Research Team, at Kasdi Merbah University of Ouargla, Algeria.

I sincerely thank all who contributed, directly or indirectly, to the successful completion of this doctoral work.

My deepest gratitude goes to my supervisor, **Mr. Khalfallah BENBELGACEM**, for his exceptional guidance, support, and constructive feedback throughout this research. I also thank my co-supervisor, **Mr. Kamal Eddine AIADI**, for his valuable advice and unwavering support.

I am grateful to **Mr. Omar BENTOUILA**, Head of the LENREZA Laboratory, for his guidance and encouragement, which greatly contributed to the progress of this research. Special thanks to **Mr. Abderrahim ACHOURI**, Chairman of the thesis committee, for his expertise and valuable contribution to the evaluation of this work.

I extend my gratitude to the members of the thesis examination committee: **Mr. Omar BENTOUILA**, **Mr. Lazhar BENMEBROUK**, **Mr. Mebrouk GHOUGALI**, and **Mr. Farhat RAHOUMA**, for their insightful comments and constructive suggestions.

Finally, I warmly thank my family, friends, and colleagues for their continuous support, encouragement, and understanding throughout this doctoral journey.

Abstract

One-dimensional photonic crystals (1D–PhCs) enable precise spectral control via photonic band gaps and defect-mode resonances. This thesis develops and evaluates a compact biosensing platform based on a quarter-wave SiO_2/TiO_2 multilayer with a central defect cavity that hosts the analyte. Using a transfer-matrix formulation, we derive transmission and reflection spectra under lossless conditions and quantify sensing performance through sensitivity (S), quality factor (Q), figure of merit (FoM), and signal-to-noise ratio (SNR). We examine how the defect thickness (d_0), the number of bilayers (N), and the incidence angle (θ) govern resonance position and linewidth.

Parametric analysis shows that increasing d_0 introduces additional cavity modes and can sharpen resonances, while larger N improves spectral selectivity and Q. Oblique incidence provides a practical knob to further narrow the resonance with a predictable blue shift. Focusing on clinically motivated detection of blood constituents, the device tracks refractive-index changes associated with human blood components and, in particular, variations in hemoglobin concentration. An optimized configuration (N=7, d_0=10D, θ=20°) yields narrow defect resonances with $Q \approx 2.6 \times 10^4$–$3.9 \times 10^4$ and sensitivity $S \approx 476$ nm/RIU. Across a representative hemoglobin range, the resonance wavelength red-shifts by $\sim$ 17.6 nm (from $\sim$ 771.6 nm to $\sim$ 789.2 nm), while maintaining FWHM on the order of 0.02–0.03 nm, enabling high-resolution discrimination of physiologically relevant changes.

These results confirm that defect-engineered 1D–PhCs, realized with standard dielectric stacks, offer a simple, low-cost, and high-performance route to optical biosensing. The framework and guidelines reported here support dispersion-aware design, tolerance analysis, and further improvements via impedance matching and cavity-mode tailoring.

Keywords: transmittance spectrum, optical properties, SiO2/TiO2, VIS wavelength, human blood, biosensor, transfer matrix method

ملخص

تُمكّن البلّورات الفوتونية أحادية البعد (1D–PhCs) من التحكم الطيفي الدقيق عبر فجوات الحزمة الفوتونية ورنينات الأنماط العيبية. يطوِّر هذا البحث ويقيّم منصة استشعار حيوي مدمجة تعتمد على طبقات متناوبة من TiO_2/SiO_2 ذات ربع طول موجي، تحتوي في مركزها على تجويف عيبي يُوضَع فيه المُحلَّل. باستخدام صياغة مصفوفة النقل، نحسب أطياف النفاذية في ظروف عديمة الفقد ونُكمّم أداء الاستشعار من خلال الحساسية (S) ومعامل الجودة (Q) ومعامل الكفاءة (FoM) ونسبة الإشارة إلى الضوضاء (SNR). ندرس كيف تؤثر سماكة العيب (d_0) وعدد الأزواج الثنائية (N) وزاوية السقوط (θ) في موقع الرنين وعرضه الطيفي.

يُظهر التحليل البارامتري أن زيادة d_0 تُدخل أنماط تجويف إضافية وقد تُحسّن حدة الرنين، بينما يؤدي ارتفاع N إلى تعزيز الانتقائية الطيفية وزيادة Q. كما توفّر الزاوية المائلة أداة عملية لتضييق الرنين أكثر مع انزياح نحو الأطوال الموجية الأقصر. في سياق الكشف السريري عن مكوّنات الدم، يتتبع الجهاز التغيرات في قرينة الانكسار المرتبطة بمكوّنات دم الإنسان، وبخاصة تغيرات تركيز الهيموغلوبين. يُظهِر التكوين الأمثل (θ=20° ,d_0=10D ,N=7) رنينات عيبية ضيقة بمعامل جودة $Q \approx 2.6 \times 10^4$–$3.9 \times 10^4$ وحساسية $S \approx 476$ nm/RIU. عبر نطاق تمثيلي لتركيز الهيموغلوبين، ينزاح طول موجة الرنين نحو الأحمر بمقدار ~ 17.6 nm (من $\sim$ 771.6nm إلى $\sim$ 789.2nm)، مع بقاء عرض النصف الأقصى (FWHM) في حدود $0.02 - 0,03nm$، مما يتيح تمييزاً عالي الدقة للتغيرات الفسيولوجية ذات الصلة.

تؤكد هذه النتائج أن البلّورات الفوتونية أحادية البعد المُهندسة بالعيوب، والمحققة عبر تراكيب عازلة قياسية، تتيح نهجاً بسيطاً ومنخفض التكلفة وعالي الأداء للاستشعار البصري الحيوي. يوفر الإطار والإرشادات المعروضة هنا أساساً لتصميم واعٍ للتشتت، وتحليل التحمّل، وتحسينات إضافية من خلال مطابقة الممانعة وتشكيل أنماط التجويف.

الكلمات المفتاحية: طيف النفاذية، الخصائص البصرية، SiO2/TiO2، الطول الموجي المرئي، دم الإنسان، المستشعر الحيوي، طريقة مصفوفة النقل.

Contents

List of Figures

List of Tables

List of Abbreviations

Abbreviation	Description
PhCs	Photonic crystals
PBG	Photonic band gaps
1D PhCs	One-dimensional photonic crystals
2D PhCs	Two-dimensional photonic crystals
3D PhCs	Three-dimensional photonic crystals
TMM	Transfer Matrix Method
FDTD	Finite-Difference Time-Domain method
PWE	Plane Wave Expansion method
DBR	Dielectric Bragg reflector
RI	Refractive index
TE	Transverse Electric polarization (s-polarization)
TM	Transverse Magnetic polarization (p-polarization)
SNR	Signal-to-noise ratio
FOM	Figure of merit
FWHM	Full width at half maximum

List of Symbols

Symbol	Description
E	Electric field vector
H	Magnetic field vector
D	Electric displacement field ($\mathbf{D} = \varepsilon_0 \varepsilon_r \mathbf{E}$)
B	Magnetic flux density ($\mathbf{B} = \mu_0 \mathbf{H}$)
ε_0	Permittivity of free space
μ_0	Permeability of free space
ε_r	Relative permittivity of the medium
k	Magnitude of the wave vector
ω	Angular frequency
λ	Wavelength in vacuum
n	Refractive index of the medium
c	Speed of light in vacuum ($c = 1/\sqrt{\mu_0 \varepsilon_0}$)
ρ_s	Surface charge density
J_s	Surface current density
$\hat{n}$	Unit normal vector to the surface
θ_i	Angle of incidence
θ_r	Angle of reflection
θ_t	Angle of transmission
r_{jk}	Reflection amplitude coefficient between media j and k
t_{jk}	Transmission amplitude coefficient between media j and k
j, k	Indices of incident and transmitted media
M	Total transfer matrix of the multilayer structure
D_l	Interface matrix of the l-th layer
P_l	Propagation matrix of the l-th layer
D_s	Substrate matrix
T	Power transmittance
R	Power reflectance
S	Sensitivity (nm/RIU)

Symbol	Description
Q	Quality factor
$\Delta\lambda_{\text{res}}$	Resonance wavelength shift
Δn	Change in refractive index
λ_{res}	Resonance wavelength
d_1	Thickness of the first layer
d_2	Thickness of the second layer
d_0	Defect layer thickness
λ_c	Central (design) wavelength
D	Lattice period ($D = d_1 + d_2$)
N	Number of periods
n_{bp}	Refractive index of blood plasma
n_{wb}	Refractive index of white blood cells
n_{hb}	Refractive index of hemoglobin
n_{rb}	Refractive index of red blood cells
C_{HB}	Hemoglobin concentration (g/dL)

General Introduction

The advent of photonic crystals (PhCs), a class of engineered materials carefully crafted to manipulate and control the propagation of electromagnetic waves with high precision, has significantly changed the field of optics [1–5]. These periodic dielectric structures exhibit distinctive optical properties, most notably the presence of photonic band gaps (PBGs), within which light of specific frequencies is prohibited from propagating—an effect analogous to the electronic band gaps in semiconductors that regulate electron transport [6–8]. Among the various dimensional configurations, one-dimensional photonic crystals (1D PhCs) occupy a unique position due to their straightforward fabrication process and strong interference effects, which facilitate narrowband transmission, high reflection, and defect-induced resonant modes. These characteristics render 1D PhCs highly promising for numerous photonic applications, including optical filters, high-reflectivity mirrors, distributed-feedback lasers, display technologies, and particularly label-free optical biosensing, where even minute refractive-index variations must be detected with exceptional accuracy [9–15].

Despite significant advancements, several critical challenges persist. Firstly, the translation of idealized band-gap concepts into manufacturable multilayers necessitates a thickness design that is cognizant of dispersion, alongside robust modeling that considers angle, polarization, and loss. Secondly, optimizing sensing performance requires a balance between mode confinement, to enhance resonance sharpness, and the issues of spectral crowding and insertion loss. Lastly, clinical translation necessitates designs with figures of merit that are resilient to parameter drift and fabrication tolerances.

Objectives. This thesis aims to (i) select a rigorous and efficient modeling pipeline for one-dimensional photonic crystals (1D PhCs), (ii) derive design principles that correlate structural parameters—such as index contrast, period number, defect thickness, and angle of incidence—with spectral metrics, including band-gap width, resonance position, and linewidth, and (iii) engineer a defect-cavity 1D PhC as a refractive-index biosensor optimized for detecting variations in human blood constituents, with a particular focus on hemoglobin.

Methodological approach. This research utilized the **Transfer Matrix Method (TMM)** in `Python` to model the propagation of electromagnetic waves through a one-dimensional photonic crystal (1D PhC) made up of alternating SiO_2/TiO_2 layers, which

include a central defect cavity. Dispersion models for SiO_2 and TiO_2 were employed to design a quarter-wave thickness centered around a specific wavelength in the visible to near-infrared spectrum. An extensive parametric analysis was conducted by altering the thickness of the defect layer, the number of periodic layers, and the angle of incidence to assess and enhance the sensor's performance in terms of sensitivity (S), quality factor (Q), signal-to-noise ratio (SNR), and figure of merit (FOM).

Scope and significance. Focusing on SiO_2/TiO_2 platforms leverages high index contrast and low absorption to obtain wide photonic band gaps and sharp defect resonances suitable for biosensing. By systematically varying the defect-layer thickness, the number of bilayers, and the incidence angle, we identify operating regimes that maximize S, Q, and FOM while mitigating peak crowding, thereby informing practical sensor layouts.

Thesis organization. In harmony with the flow of the document, the dissertation is structured as follows:

- **Chapter 1: A General Introduction to Photonic Crystals.** Presents fundamental concepts of PhCs, including dimensional taxonomies (1D/2D/3D), natural analogues, and the structural/optical properties of 1D PhCs. It surveys application domains and outlines mainstream fabrication techniques for multilayer stacks.

- **Chapter 2: Simulation Methods for One-Dimensional Photonic Crystals.** Develops the theoretical background from Maxwell's equations and details the Fresnel formalism, single-layer optics, and multilayer analysis. It formulates TMM for stratified media and summarizes FDTD and PWE for complementary verification and band-structure intuition.

- **Chapter 3: Design of a One-Dimensional Photonic Crystal Biosensor.** Specifies the SiO_2/TiO_2 stack, quarter-wave thickness rules, and the insertion of a central defect cavity hosting the analyte. It defines performance metrics (S, Q, SNR, FOM) and establishes an energy-conserving TMM framework for transmittance/reflectance spectra.

- **Chapter 4: Results and Analysis of the Photonic Crystal Biosensor.** Reports parametric studies over defect thickness, period number, and incidence angle, then applies the optimized design to detect hemoglobin variations, quantifying sensitivity and spectral selectivity against literature baselines.

Contributions and outlook. The thesis provides a compact, dispersion-aware TMM pipeline for 1D PhC sensor design, identifies parameter regimes that jointly improve S, Q, and FOM, and demonstrates clinically relevant discrimination of hemoglobin-level changes. The concluding section discusses limits and prospective extensions, in-

cluding impedance-matched terminations, hybrid material stacks, and tolerance-aware design for robust fabrication.

Chapter 1

A General Introduction to Photonic Crystals

1.1 Introduction

Photonic crystals (PhCs) are optical nanostructures with a periodic arrangement that regulates light propagation, similar to the way atomic lattices affect electron movement in solids. This chapter presents the fundamental principles of PhCs, exploring their various forms and natural examples. It examines the structural and optical characteristics of one-dimensional photonic crystals (1D PhCs) and their diverse applications, such as filters, lasers, and sensors. Additionally, it highlights fabrication methods including physical and chemical vapor deposition, sol–gel processing, and nanofabrication techniques. Overall, this chapter lays the foundational knowledge needed to understand the principles, properties, and production techniques of PhCs.

1.2 Photonic Crystals

Photonic crystals (PhCs) are structures defined by a periodic arrangement of materials with differing refractive indices (RI). This periodicity, usually on the scale of optical wavelengths, enables the manipulation of light in ways not possible with traditional homogeneous materials. The periodic variation of the dielectric constant within these structures is essential to their unique optical characteristics, leading to effects such as omnidirectional reflection and the formation of photonic band gaps (PBGs), where light propagation is restricted.

1.2.1 Types of PhCs

PhCs are primarily categorized based on the dimensionality of their periodic structure, which determines the degree to which they can confine and control light. This

section provides an overview of one-dimensional (1D), two-dimensional (2D), and three-dimensional (3D) PhCs, highlighting their structures, properties, fabrication challenges, and applications.

1.2.1.1 One-Dimensional Photonic Crystals

One-dimensional photonic crystals (1D PhCs) are optical structures characterized by a periodic arrangement of layers composed of materials with alternating RI. These structures operate on the principles of constructive and destructive interference of electromagnetic waves, resulting in the formation of a PBG that selectively blocks certain wavelengths while allowing others to pass [16].

Although 1D PhCs exhibit periodicity along only one axis, their geometrical configurations can vary; they may be flat, cylindrical, or spherical (Figure 1.1). The most common geometry is the planar structure, where thin layers are deposited on a flat substrate and used extensively in optical coatings [17]. Cylindrical 1D PhCs consist of concentric layers around a central axis and find applications in optical fibers and resonators [18]. Spherical 1D PhCs feature radially arranged layers, offering omnidirectional light control and enabling uses such as isotropic reflectors and photonic sensors [19].

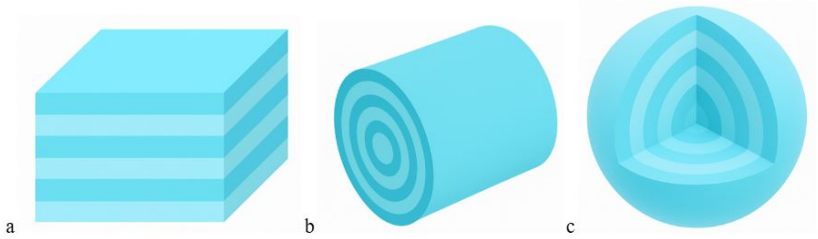

Figure 1.1: Types of 1D PhC structures: (a) planar, (b) cylindrical, (c) spherical.

Several precise fabrication techniques are used to produce 1D PhCs. Among the most prominent is the sol–gel spin-coating technique, which enables the deposition of alternating thin layers with high control over thickness and RI [20, 21]. Advanced fabrication methods—such as direct laser writing and two-photon polymerization—have also been developed to introduce defect layers within the periodic structure [22].

1.2.1.2 Two-Dimensional Photonic Crystals

Two-dimensional photonic crystals (2D PhCs) consist of periodic arrangements of dielectric materials, such as arrays of air holes or dielectric rods, organized into specific lattice geometries including square, triangular, or hexagonal patterns (Figure 1.2). These periodic structures give rise to PBGs—frequency ranges in which electromag-

netic wave propagation is prohibited within the plane of the crystal. This feature allows for precise manipulation of light in planar photonic devices [23–26].

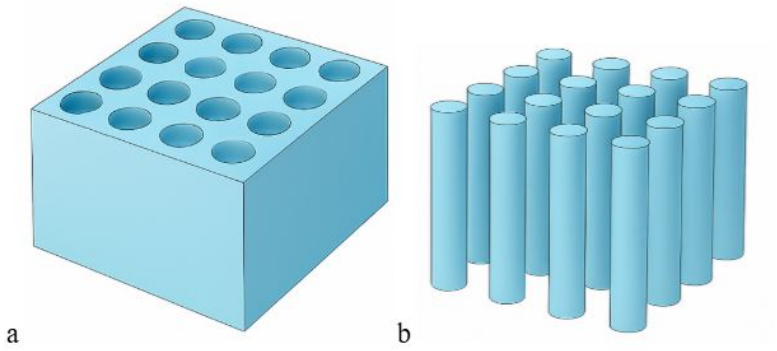

Figure 1.2: 2D PhCs structures with different lattice geometries.

The optical performance of 2D PhCs is highly dependent on the accuracy of the fabrication process. Photolithography and etching are among the most widely used techniques, enabling the realization of highly precise periodic structures necessary for well-defined PBGs. Recent advancements focus on improving etching resolution, developing advanced lithographic processes, and integrating novel dielectric and semiconductor materials to enhance scalability and reproducibility [27, 28].

1.2.1.3 Three-Dimensional Photonic Crystals

Three-dimensional photonic crystals (3D PhCs) are unique materials characterized by a periodic RI modulation in all three spatial dimensions. This full 3D periodicity enables complete control of light propagation—an ability not achievable with 1D or 2D counterparts. Various engineered and self-assembled structures exist (Figure 2.1), each offering distinct optical capabilities. The woodpile structure, composed of orthogonally stacked dielectric rods, is among the most widely studied [29]. Opal PhCs form through self-assembly of monodisperse colloidal particles [30], while tetragonal PhCs typically consist of two perpendicular sets of air pores embedded in a dielectric matrix [31].

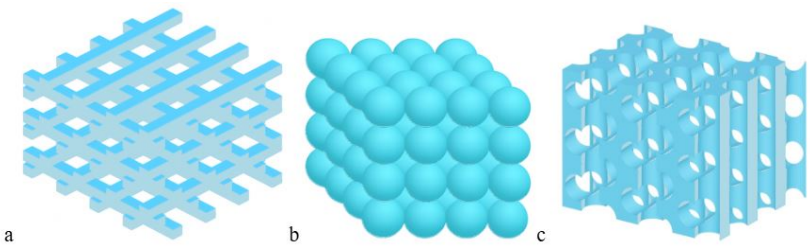

Figure 1.3: 3D PhC structures: (a) woodpile, (b) opal, (c) tetragonal.

Fabricating 3D PhCs requires advanced methods to achieve precise periodicity and the desired optical response. Multi-beam interference lithography provides large-area, high-precision structuring, whereas direct laser writing (DLW) enables fabrication of complex microarchitectures [32]. Layer-by-layer stacking offers excellent structural fidelity through sequential alignment [33]. Colloidal self-assembly provides a scalable, cost-effective route for visible and infrared structures [34]. Additionally, focused ion beam (FIB) lithography offers nanometer-scale accuracy, making it ideal for prototyping and local structural refinement [35].

1.2.2 Difference Between photonic crystals and Atomic Crystals

The analogy between PhCs and atomic crystals is insightful, yet crucial distinctions exist. In atomic crystals, atoms or molecules are arranged in a periodic lattice structure at the atomic scale (angstroms), which influences the propagation of electrons and determines the material's electronic properties, such as conductivity. This periodicity gives rise to electronic band gaps, forbidding certain electron energy levels [36–38].

Conversely, PhCs operate at a much larger scale, typically nanometers to micrometers, and are engineered to manipulate photons (light) rather than electrons. Their periodic variation lies in the dielectric constant or RI. While both systems exhibit band gaps, the fundamental difference lies in the particles involved: electrons are massive fermions, whereas photons are massless bosons [39, 40]. PhCs achieve their band gaps through classical interference effects of electromagnetic waves interacting with the periodic dielectric structure, rather than quantum mechanical interactions that govern electronic band gaps. This allows PhCs to control light propagation in a manner analogous to how atomic crystals control electron waves, but without the need for electronic confinement [41].

1.2.3 photonic crystals in Nature

Natural PhCs are responsible for the phenomenon of structural coloration observed in a wide range of biological systems. Unlike pigments, which rely on selective absorption, these structures manipulate light through interference, diffraction, and scattering. A well-known example is the iridescent wings of *Morpho* butterflies, which contain one-dimensional multilayer nanostructures that selectively reflect certain wavelengths of light, producing their characteristic vivid blue color. Similarly, periodic micro- and nanostructures in bird feathers and beetle shells give rise to striking hues and metallic appearances, often exhibiting one-dimensional, two-dimensional, or even complex quasi-three-dimensional photonic behaviors.

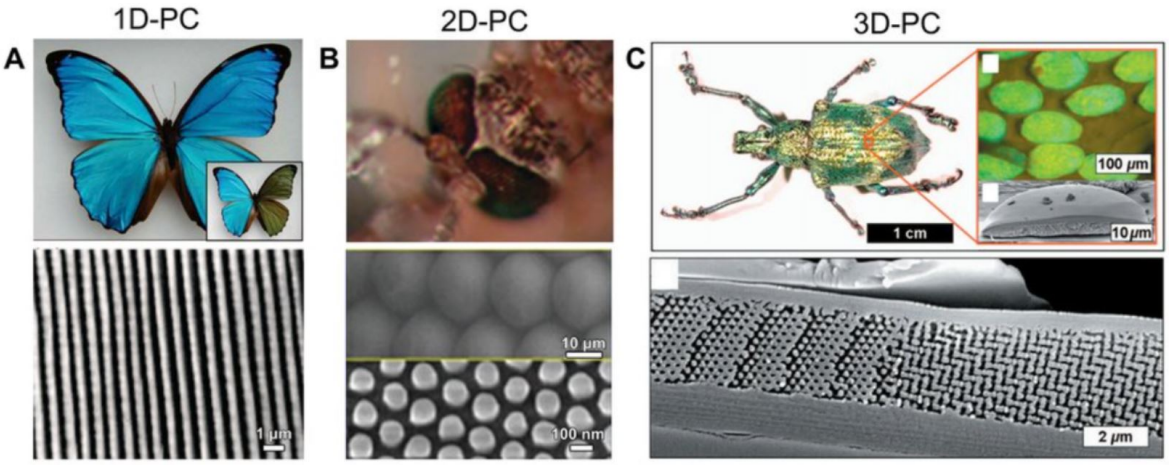

Figure 1.4: An intricate view of a butterfly wing, illustrating the natural multilayer nanostructures responsible for its vibrant, structural colors[42].

1.3 Physical Properties of One-Dimensional photonic crystal

1.3.1 Structural Properties

The very essence of a 1D PhC lies in its meticulously arranged structure. Two critical structural parameters dictate how these crystals interact with light: their periodicity and the thickness of their constituent layers.

1.3.1.1 Periodicity (N)

Periodicity, also referred to as N, represents the count of repeating unit cells within a real PhC structure. Typically, each unit cell is composed of at least two alternating layers made from different materials. Additionally, another key parameter that significantly influences the optical characteristics of a crystal is the quantity of these repeating units or periods. A higher number of periods results in a more well-defined photonic band gap; consequently, the reflectivity within this forbidden band increases significantly with increasing number of periodic layers. This improved control over light propagation makes the crystal better applicable whenever accurate optical filtering is required or high reflectivity is needed almost like that from a very good optical mirror [43].

1.3.1.2 Layer Thickness

The thickness of individual layers is an important parameter that defines the position as well as the width of the photonic band gaps. Therefore, to do this optimally, they

are most often designed at optical thicknesses corresponding to a quarter wavelength of light intended for use, i.e., $\lambda/4$, tuning which makes possible strong Bragg reflection responsible for the generation of photonic band gaps [44].

Engineers can move the band gap to particular wavelengths by controlling layer thicknesses accurately; hence, 1D PhCs find obligatory usage in applications where narrowband filters and highly sensitive sensors are to be used or even specific laser designs [45].

1.3.2 Optical Properties

The most celebrated characteristics of 1D PhCs are their optical properties, which enable unprecedented control over light. These properties are intrinsically linked to the periodic variation of the RI within the crystal.

1.3.2.1 Refractive Index (RI)

The difference in RI between successive layers is basically what 1D PhCs operate on. High- and low-dielectric-constant materials are juxtaposed to realise these periodic variations [46]. A greater difference of RL between adjacent layers results in a wider and more pronounced photonic band gap that reflects more effectively. It is this periodic modulation of the RI that enables coupling between forward- and backwards-propagating waves so as to realise both types of interference–constructive and destructive–that is the very foundation of the crystal's ability to control light propagation.

1.3.2.2 Photonic Band Gap

A photonic band gap (PBG) is analogous to electronic band gaps found in semiconductors. It represents a range of wavelengths where light cannot propagate through a crystal. This phenomenon occurs due to the constructive interference of light waves that are reflected at the periodic boundaries between layers. The specific location and breadth of the PBG are entirely dictated by the periodicity and thickness of the layers, as well as the RI contrast between the materials involved [47]. By adjusting these parameters, it is possible to reflect or confine certain wavelengths of light, paving the way for the development of highly specialized optical components [48].

1.3.2.3 Transmittance and Reflectance

A PBG has its immediate manifestation in the transmittance and reflectance spectra of 1D PhCs [49]. In the region of the band gap, reflectance reaches its highest value possible with near-total reflection for large values of periods (N), while transmissivity

through the structure falls to essentially zero. Outside the band gap, light is freely transmitted through the structure. These are highly exploited properties in mirror coatings, highly selective optical filters, and optical waveguides, among other applications, with precise control over layer thicknesses and RI to tailor transmission spectra for specific functionalities that enable designing devices having exact optical responses.

1.3.2.4 Absorption

The main design goal for 1D PhCs is essentially the control of light propagation (reflection as well as transmission), but absorption comes into play based on material composition. Ideally, low-loss dielectrics are used so that absorption can be minimized in maximizing efficiency. However, if absorbing materials are included—intended only for special applications like photothermal conversion or as an incidental property of the materials being used—absorption may also affect the actual band gap and general transmission. High absorption will not allow transmittance to reach its maximum value; it damps resonant states and hence affects device performance and efficiency.

1.3.3 Other Physical Properties

While their optical prowess is primary, 1D PhCs also exhibit a range of other physical properties—electrical, thermal, and mechanical—that are crucial for their integration into practical devices and their long-term stability.

1.3.3.1 Electrical Properties

Though basically created for optical regulation, the 1D PhCs acquire electrical significance when they contain a semiconductor or conductive layer [50]. In such instances, the periodic structure can be used to perform electronic transport property modulation at the nanoscale, hence possible changes in carrier mobility and capacitance. This leads to the invention of electrically tunable PhCs that may realize functionalities such as voltage-controlled switching and electro-optic modulation or be integrated into very complex electronic-photonic circuits. For example, conductive polymers or liquid crystals may be included so that tunability is introduced by means of electrical control.

1.3.3.2 Thermal Properties

Thermal conductivity essentially depends on those materials 1D PhCs are made of. In general, the layered periodic structure permits modulation of thermal conductivity due to phonon scattering at interfaces. High thermal stability would, therefore, assist in not varying the exact thicknesses of the layers and their RI at any operating temperature by keeping optical performance constant. Apart from stability, tunability can also be

realized with materials presenting a RI variation as a function of temperature based on thermo-optic effects which shift the PBG with temperature proposed by [51]. This material may then find application in thermal sensors or intelligent thermal management systems.

1.3.3.3 Mechanical Properties

The mechanical properties of 1D PhCs refer to strength, elasticity, and the adhesion between the layers that build up the structure. These particular features become very important in real use and applications of such systems whenever dynamic or static mechanical strains are imposed on them, for example when used as flexible structures or wearable devices. Strength will also determine how easy it is to fabricate and is also useful when considering long-term durability and reliability aspects of the device. Besides this, mechanical stress can sometimes tune the optical characteristics of 1D PhCs by changing their RI through elasto-optic or piezo-optic effects thereby resulting in mechanically tunable optical devices [52].

1.4 Applications of One-Dimensional Photonic Crystals

1D PhCs are extensively utilized photonic structures, renowned for their simplicity, versatility, and exceptional capacity to manipulate light propagation through interference effects and PBG. These structures have been widely applied across various domains, including telecommunications, sensing, energy harvesting, and integrated photonics. The periodic arrangement of alternating layers with differing RI facilitates highly selective optical responses, particularly in controlling reflection, transmission, and localization of light at specific wavelengths.

1.4.1 Optical Filters

1D PhCs are critically important in advancing optical filter technologies due to their inherent capability to selectively transmit or reflect specific wavelengths. Their structural precision enables effective implementation in various filtering applications. Particularly in narrowband optical filtering, 1D PhCs facilitate the production of filters characterized by high spectral selectivity and minimal transmission losses. The deliberate introduction of defect layers within these structures generates sharp defect-mode resonances, highly advantageous for precision-dependent applications such as interferometry and high-resolution optical communication systems [53].

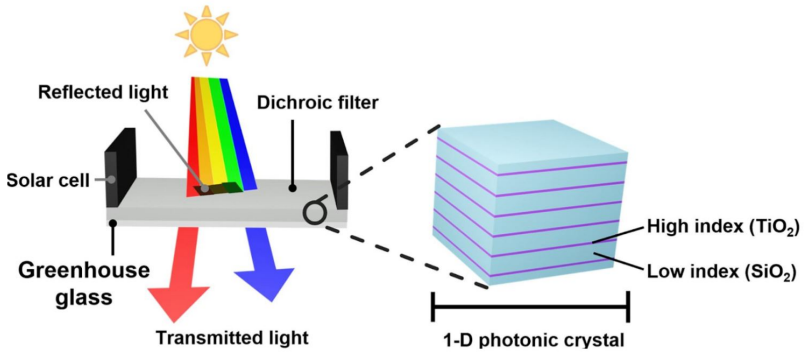

Figure 1.5: Schematic Diagram of a 1D PhC Integrated as a Dichroic Filter in Solar-Greenhouse Systems [54].

This schematic in Figure 1.5 illustrates a practical example of a dichroic 1D PhC filter composed of alternating TiO_2 and SiO_2 layers. The structure selectively reflects infrared wavelengths toward photovoltaic cells while transmitting photosynthetically active radiation (PAR) into a greenhouse. This dual functionality enables simultaneous renewable energy generation and optimal crop illumination, highlighting the potential of 1D PhCs in sustainable agricultural and energy applications.

1.4.2 Dielectric Mirrors

1D PhCs are integral to Bragg mirrors, which rely on periodic RI variations to reflect specific light wavelengths. These mirrors achieve high-efficiency, lossless reflectivity through PBG, distinguishing them from traditional metallic mirrors. 1D PhC-based mirrors, including flexible and omni-directional types, offer broad applicability in optical devices like waveguides, resonant cavities, and photodetectors [55].

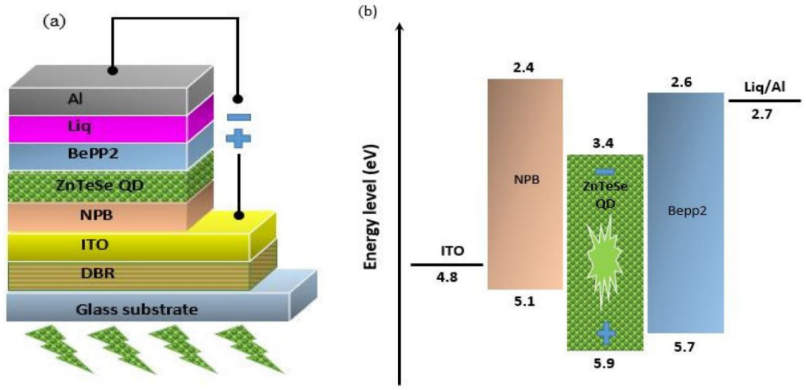

Figure 1.6: Schematic Structure of a Quantum Emission Device Supported by a Dielectric Bragg Reflector (DBR) [56].

The figure 1.6 illustrates a light-emitting device that incorporates ZnTeSe quantum

dots, with a dielectric Bragg reflector (DBR) to improve vertical light coupling. The device's architecture includes a glass substrate, DBR, hole transport layer (NPB), electron transport layer (BePP2), and the quantum dot emissive layer. Part (b) displays an energy level diagram that demonstrates the alignment facilitating electron and hole injection into the quantum dots, highlighting the essential function of dielectric mirrors in enhancing the light-emission efficiency of quantum dot light-emitting diodes (QD-LEDs)[56].

1.4.3 Sensor

1D PhCs have emerged as powerful tools in optical sensing due to their high sensitivity to RI variations and the ability to support engineered PBGs. These properties enable precise detection of environmental changes and target analytes in applications such as biosensing, chemical detection, and environmental monitoring. The sensing mechanism relies on the modulation of optical response, such as transmission or resonance, caused by RI shifts, with defect modes further enhancing sensitivity and selectivity [57].

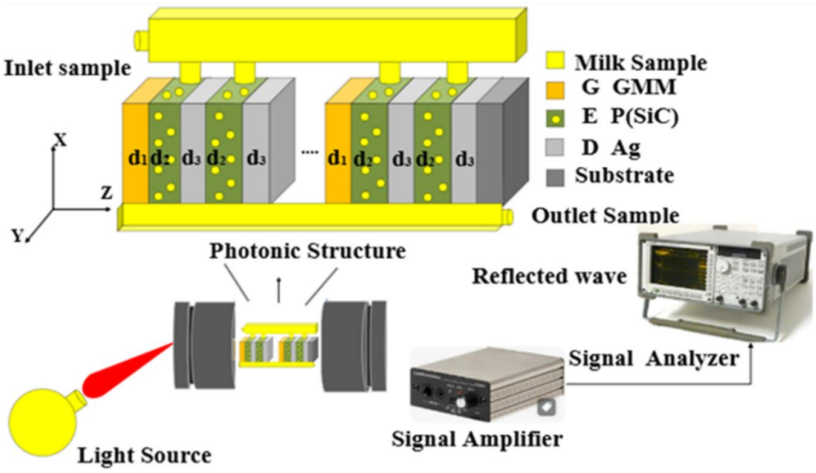

Figure 1.7: 1D PhCs Sensor for Detecting Fat Concentration in Milk Samples [58].

The figure 1.7 illustrates a schematic of a 1D PhC sensor designed for non-invasive milk fat content detection. The sensor features alternating layers of metamaterials (HMMs and GMMs) with varying thicknesses and RI. As the milk sample interacts with the photonic structure, it induces a shift in the reflected optical signal, which is analyzed using a signal amplifier and spectrum analyzer. The high RI sensitivity of the 1D PhC enables precise detection of fat concentration variations through spectral changes.

1.4.4 Lasers

1D PCs are integral to modern laser technologies, enabling precise light manipulation through PBGs. In distributed feedback (DFB) lasers, 1D PCs serve as Bragg reflectors, providing wavelength-specific feedback that stabilizes output and enhances spectral purity, crucial for telecommunication and sensing applications [59]. In vertical-cavity surface-emitting lasers (VCSELs), 1D PCs form DBRs that facilitate efficient vertical light emission, making VCSELs ideal for high-density optical interconnects and data communication.

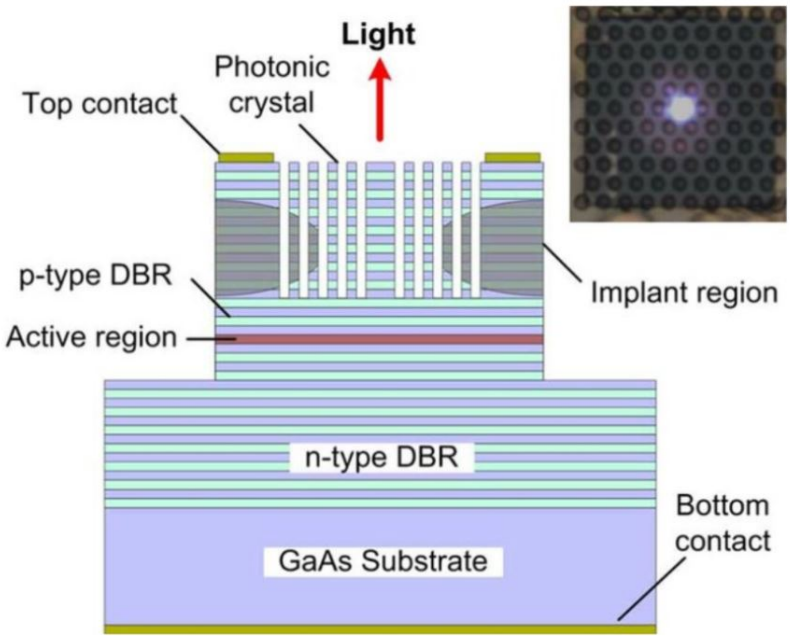

Figure 1.8: Cross-sectional schematic of a PhC vertical-cavity surface-emitting laser (PC-VCSEL) [60].

The figure 1.8 illustrates a VCSEL design with a 1D PhC etched into the top distributed Bragg reflector (DBR), forming a lateral resonant cavity for mode selection. This design improves beam quality, spectral purity, and efficiency by providing vertical and lateral feedback, making it ideal for compact, high-performance, and CMOS-compatible light sources.

1.4.5 Photovoltaics and Energy Applications

1D PhCs are pivotal in enhancing light management for photovoltaic and energy systems by engineering PBGs to control light propagation. They are particularly useful in solar technologies, improving light absorption, reducing optical losses, and increasing energy conversion efficiency, especially in thin-film solar cells where material thickness

is limited. 1DPCs also serve as spectral filters in thermophotovoltaic (TPV) systems and as anti-reflective coatings and back reflectors to enhance absorption [61].

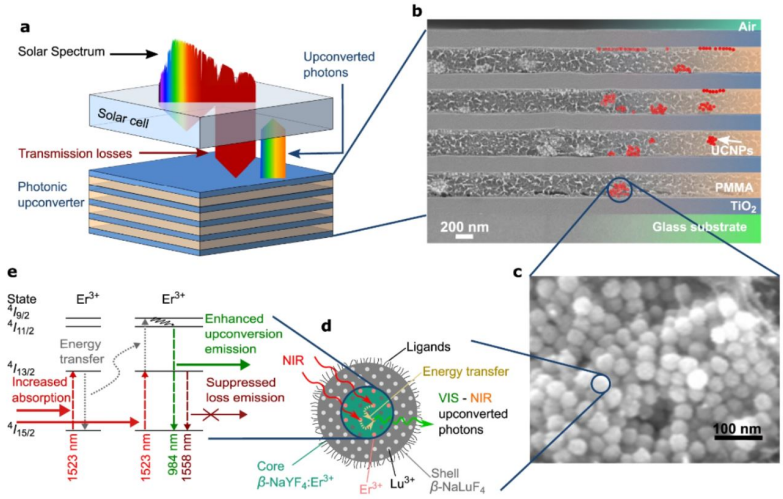

Figure 1.9: One-Dimensional Photonic Upconverter for Solar Energy Enhancement [62].

The figure 1.9 shows a photonic upconverter device that integrates a 1D PhC with upconverting nanoparticles (UCNPs) to convert near-infrared photons into visible light, improving solar cell efficiency. The TiO_2/PMMA multilayer design enhances upconversion by utilizing light confinement and PBG effects.

1.4.6 Integrated Photonics

1D PhCs are crucial for advancing integrated photonic circuits, as their periodic RI profile allows precise light manipulation in compact, subwavelength-scale structures. These structures enable the design of essential optical components such as filters, mirrors, waveguides, and logic elements, supporting the miniaturization and performance optimization of photonic systems, particularly in silicon photonics [63]. Their compatibility with CMOS fabrication processes facilitates integration into existing microelectronic platforms, making 1D PhCs a cost-effective and scalable solution for hybrid photonic-electronic systems.

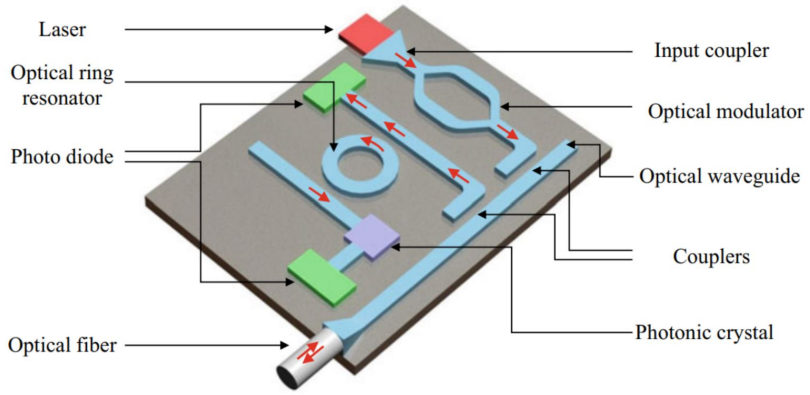

Figure 1.10: Schematic Diagram of a Photonic Integrated Circuit (PIC) Incorporating a 1D PhC [64].

The figure 1.10 shows the layout of a photonic integrated circuit (PIC) that integrates multiple optical components, including a 1D PhC for wavelength-selective control, filtering, and signal routing. This integration highlights the PhC's role in compact, CMOS-compatible platforms, enabling scalable and multifunctional optical circuits.

1.4.7 Electronic Displays

Electrically tun-able PhC displays represent a significant advancement in display technologies, offering dynamic color modulation without external back-lighting. These displays work by modulating the PBG through electric fields, which induce structural changes in the PhC layers, altering the wavelengths of reflected light. The two main methods of tuning include electrical actuation, which adjusts the periodic layers for color tuning across a wide spectral range, and RI modulation, where liquid crystal components embedded within the structure enable precise, reversible color control [65].

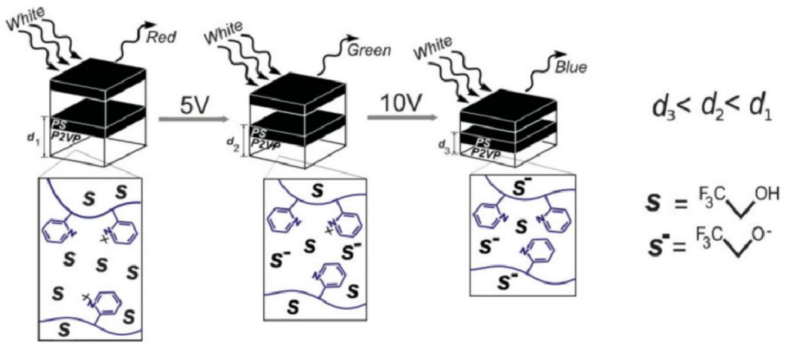

Figure 1.11: Mechanism of electrochemically tun-able color response in multilayer 1D PhC structures for display applications [66].

The figure 1.11 depicts the mechanism of color adjustment in a one-dimensional

PhC composed of PS–P2VP block copolymer layers. Upon the application of an external voltage, electrochemical oxidation leads to the selective expansion of the P2VP domains. This process modifies the periodicity and RI of the layers, resulting in a shift of the PBG and a change in the visible color, which holds promise for low-power, high-resolution display applications.

1.4.8 Optical Switches

1D PhCs serve as a vital platform for the development of optical switching devices, which are essential in high-speed optical communication and signal processing systems. These devices leverage nonlinear optical effects in integrated materials within the photonic structure to control the propagation of light. When the intensity of incident light exceeds a certain threshold, the optical properties of the active medium—such as the RI or absorption coefficient—undergo nonlinear changes. This enables the optical switch to toggle between transmissive (ON) and reflective (OFF) states [67].

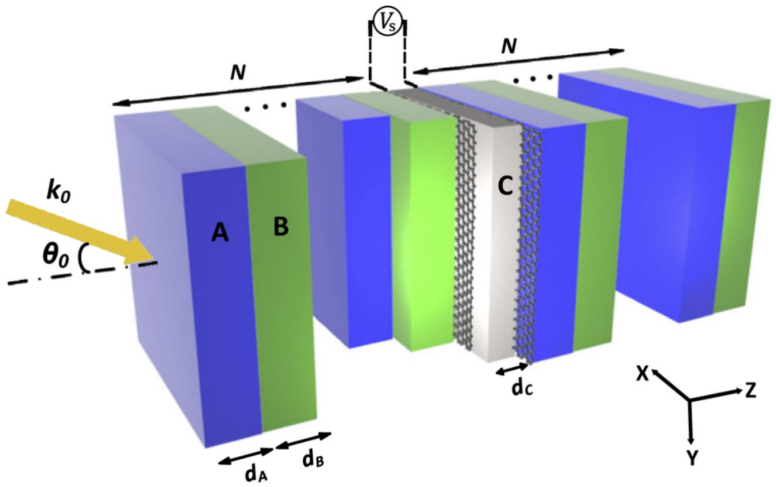

Figure 1.12: Perspective view of the optical switch with applied voltage [68].

This figure 1.12 illustrates the setup of an optical switch that employs a 1D PhC. The design features alternating dielectric layers (A and B) with a central anisotropic graphene C defect layer. Applying a voltage (V_s) across the graphene layers alters the optical characteristics of the structure, allowing the device to toggle between transmissive and reflective modes. The arrow shows the direction of the incident light (k_0) as it enters at an angle θ_0. This arrangement facilitates dynamic, voltage-driven switching, making it ideal for high-performance optical uses.

1.5 Manufacturing Methods for One-Dimensional Photonic Crystals

Several fabrication methodologies have been developed for 1D PCs, each with distinct advantages and inherent limitations. Since 1D PCs are essentially periodic multilayer structures, their fabrication is strongly related to thin-film deposition techniques that enable precise control over layer thickness and RI contrast. These methods are crucial in tailoring the optical response, such as reflectance, transmittance, and PBG properties, according to specific application requirements.

1.5.1 Physical Vapor Deposition (PVD)

Physical vapor deposition is one of the most widely employed approaches for fabricating multilayer PhCs. Techniques such as thermal evaporation and electron-beam evaporation allow deposition of alternating dielectric layers with nanometer-scale thickness control. The advantages of PVD include relatively low cost, compatibility with a wide range of materials, and the ability to fabricate large-area coatings. However, challenges arise in achieving uniformity over complex substrates and in controlling interfacial roughness, which can lead to scattering losses.

1.5.2 Chemical Vapor Deposition (CVD)

Chemical vapor deposition provides a versatile route for depositing high-quality thin films with excellent adhesion and uniformity. Plasma-enhanced CVD (PECVD), for example, enables the growth of dielectric multilayers such as SiO_2/Si_3N_4 stacks, which are extensively used in optical coatings and photonic devices. The main advantages of CVD are its conformal coverage and reproducibility, while its limitations include high processing temperatures and the need for precise precursor control.

1.5.3 Sputtering Techniques

Magnetron sputtering, a form of PVD, has been widely used to deposit alternating oxide and nitride layers. This method ensures high-density films with good optical quality and environmental stability. Reactive sputtering, in particular, enables tuning of the RI by adjusting the gas composition. Nevertheless, sputtering systems can be expensive, and deposition rates are relatively low compared to evaporation-based methods.

1.5.4 Sol-Gel Processing

The sol-gel method represents a solution-based approach that enables the fabrication of multilayer dielectric coatings with controllable porosity and RI. Alternating layers can be deposited by spin-coating or dip-coating, followed by thermal treatment to remove residual solvents. Sol-gel processing offers advantages such as low cost and large-area fabrication; however, it suffers from limitations in mechanical stability and long-term durability of the layers.

1.5.5 Layer-by-Layer (LbL) Self-Assembly

This method relies on the sequential adsorption of oppositely charged polyelectrolytes or nanoparticles to build multilayered structures with nanoscale thickness control. LbL assembly provides flexibility in combining organic and inorganic components, enabling hybrid PhCs. Despite its versatility, the process is relatively slow and less suited for large-scale manufacturing.

1.5.6 Advanced Nanofabrication Approaches

Recent developments include atomic layer deposition (ALD) and molecular beam epitaxy (MBE), which offer atomic-scale precision in layer thickness and composition. ALD, in particular, is attractive for fabricating highly uniform multilayers with smooth interfaces, making it suitable for applications in optical filters and DBRs. However, these techniques are costly and often limited to small substrates.

Chapter 2

Simulation methods for one-dimensional photonic crystals

2.1 Introduction

This chapter explores the theoretical and numerical underpinnings of modeling one-dimensional photonic crystals (1D PhCs), which utilize the periodic alternation of dielectric layers to regulate light propagation. The discussion commences with an examination of Maxwell's equations and the electromagnetic boundary conditions that elucidate interference and resonance phenomena. It further illustrates how impedance mismatch and phase accumulation contribute to the formation of photonic band gaps (PBGs). The chapter delineates three primary numerical methodologies for analyzing such structures: the Transfer Matrix Method (TMM), the Finite-Difference Time-Domain method (FDTD), and the Plane-Wave Expansion method (PWE).

2.2 Propagation of Light in Dielectric Media

2.2.1 Maxwell's Equations

The fundamental description of electromagnetic wave propagation is governed by Maxwell's equations. For a linear, isotropic, and non-magnetic dielectric medium with no free charges or currents, these equations take the following form:

$$\nabla \cdot \mathbf{D} = 0 \quad \text{(Gauss's Law)} \tag{2.1}$$

$$\nabla \cdot \mathbf{B} = 0 \quad \text{(Gauss's Law for Magnetism)} \tag{2.2}$$

$$\nabla \times \mathbf{E} = -\mu_0 \frac{\partial \mathbf{H}}{\partial t} \quad \text{(Faraday's Law of Induction)} \tag{2.3}$$

$$\nabla \times \mathbf{H} = \epsilon_0 \epsilon_r \frac{\partial \mathbf{E}}{\partial t} \quad \text{(Ampère's Circuital Law)} \tag{2.4}$$

where $\mathbf{E}$ and $\mathbf{H}$ are the electric and magnetic field vectors, $\mathbf{D} = \epsilon_0 \epsilon_r \mathbf{E}$ is the electric displacement field, $\mathbf{B} = \mu_0 \mathbf{H}$ is the magnetic flux density, ϵ_0 and μ_0 are the permittivity and permeability of free space, and ϵ_r is the relative permittivity of the medium.

2.2.2 Analytical Solutions of Maxwell's Equations

By combining Maxwell's equations, we derive the electromagnetic wave equation for the electric field in a homogeneous medium:

$$\nabla^2 \mathbf{E} - \mu_0 \epsilon_0 \epsilon_r \frac{\partial^2 \mathbf{E}}{\partial t^2} = 0 \tag{2.5}$$

For a harmonic, monochromatic wave with angular frequency ω, the solution takes the form of a plane wave:

$$\mathbf{E}(\mathbf{r}, t) = \mathbf{E}_0 e^{i(\omega t - \mathbf{k} \cdot \mathbf{r})} \tag{2.6}$$

where $\mathbf{k}$ is the wave vector with magnitude $k = n\frac{\omega}{c} = n\frac{2\pi}{\lambda}$, $n = \sqrt{\epsilon_r}$ is the Refractive indices(RI), and $c = 1/\sqrt{\mu_0 \epsilon_0}$ is the speed of light in vacuum.

2.2.3 Electromagnetic Boundary Conditions at a Dielectric Interface

When an electromagnetic wave encounters the boundary between two dielectric media with RI n_1 and n_2, the incident wave undergoes partial reflection and partial transmission. The exact behavior is governed by the boundary conditions imposed by Maxwell's equations.

1. **Normal component of the electric flux density:**

$$\hat{n} \cdot (\mathbf{D}_2 - \mathbf{D}_1) = \rho_s, \tag{2.7}$$

where ρ_s is the surface charge density. In the absence of free surface charges:

$$\hat{n} \cdot \mathbf{D}_1 = \hat{n} \cdot \mathbf{D}_2.$$

2. **Normal component of the magnetic flux density:**

$$\hat{n} \cdot (\mathbf{B}_2 - \mathbf{B}_1) = 0, \tag{2.8}$$

which implies

$$\hat{n} \cdot \mathbf{B}_1 = \hat{n} \cdot \mathbf{B}_2.$$

3. **Tangential component of the electric field:**

$$\hat{n} \times (\mathbf{E}_2 - \mathbf{E}_1) = 0, \tag{2.9}$$

meaning that the tangential components of $\mathbf{E}$ are continuous across the interface.

4. **Tangential component of the magnetic field:**

$$\hat{n} \times (\mathbf{H}_2 - \mathbf{H}_1) = \mathbf{J}_s, \tag{2.10}$$

where $\mathbf{J}_s$ is the surface current density. In the absence of surface currents:

$$\hat{n} \times \mathbf{H}_1 = \hat{n} \times \mathbf{H}_2.$$

Here, $\hat{n}$ is the unit normal to the surface directed from medium 1 into medium 2.

2.3 Reflection and Transmission at Dielectric Interfaces

2.3.1 Fresnel Equations at a Dielectric Interface

The interaction of the incident wave with the dielectric interface can be further described using Fresnel equations, which determine the reflectivity and transmittance of the wave. These equations are derived by applying the boundary conditions of the electric and magnetic fields at the separating surface.

The angles θ_i, θ_r, and θ_t represent the angles of incidence, reflection, and transmission, respectively, at the interface. The RI n_1 and n_2 correspond to the incident and transmission media.

The reflectivity and transmittance coefficients are expressed as follows:

$$R_p = \left| \frac{E_{rp}}{E_{ip}} \right|^2 = \left| \frac{n_t \cos\theta_i - n_i \cos\theta_t}{n_i \cos\theta_i + n_t \cos\theta_t} \right|^2, \tag{2.11}$$

$$T_p = \frac{E_{tp}}{E_{ip}} \frac{\cos\theta_t}{\cos\theta_i} = \frac{4 n_i n_t \cos\theta_i \cos\theta_t}{(n_t \cos\theta_i + n_i \cos\theta_t)^2}, \tag{2.12}$$

$$R_s = \left| \frac{E_{rs}}{E_{is}} \right|^2 = \left| \frac{n_i \cos\theta_i - n_t \cos\theta_t}{n_i \cos\theta_i + n_t \cos\theta_t} \right|^2, \tag{2.13}$$

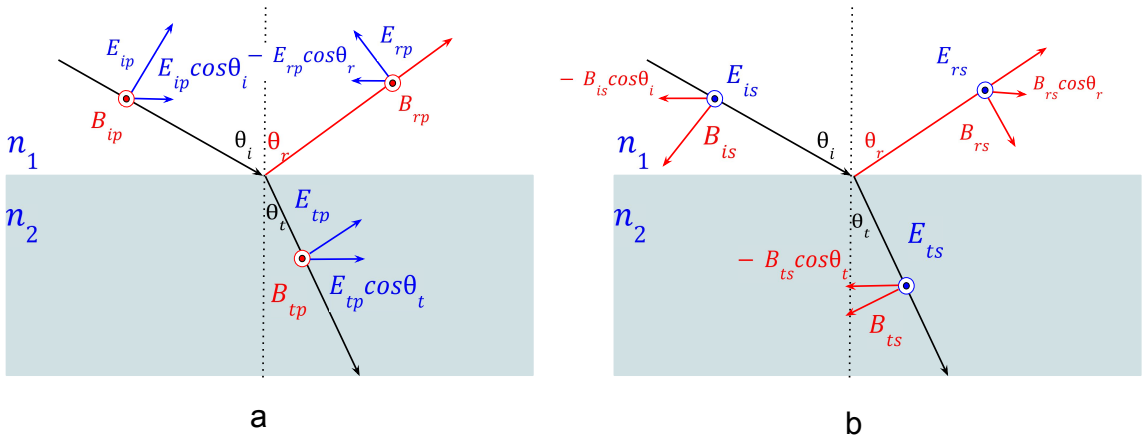

Figure 2.1: Reflection and transmission of an electromagnetic wave at the interface between two dielectrics: (a) p-polarization and (b) s-polarization.

$$T_s = \frac{E_{ts}}{E_{is}} \frac{\cos\theta_t}{\cos\theta_i} = \frac{4 n_i n_t \cos\theta_i \cos\theta_t}{(n_i \cos\theta_i + n_t \cos\theta_t)^2}. \tag{2.14}$$

2.3.2 Optical Model of a Single-Layer Thin Film

For the theoretical analysis of the reflection and transmission spectra of a single-layer thin-film system deposited on a substrate, the mathematical treatment becomes increasingly complex. In this context, the Ferry–Byron formalism provides a rigorous framework to account for the multiple reflections and interference phenomena occurring within the film (see Fig. 2.2) [69].

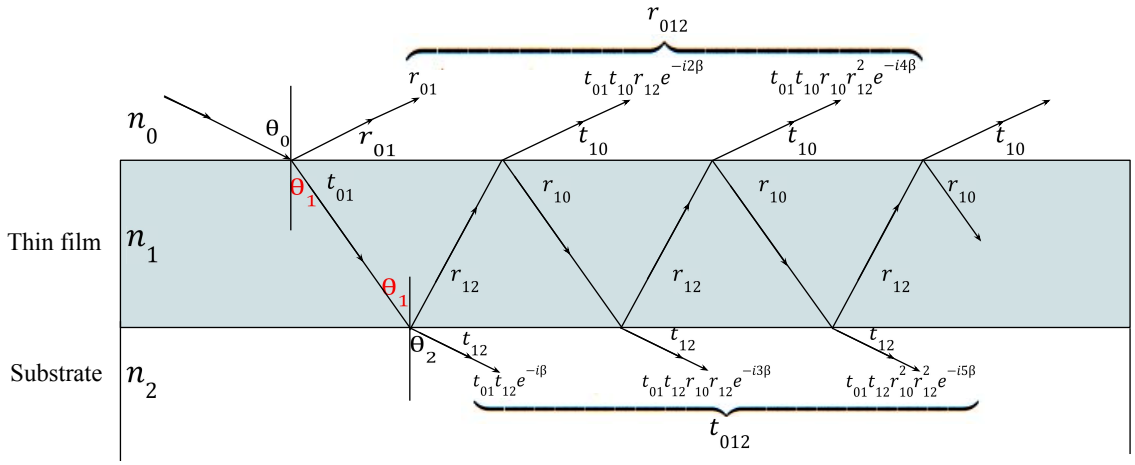

Figure 2.2: Optical model of the thin film system on a substrate.

Figure 2.2 illustrates the optical response of a thin-film/substrate system. When an incident wave impinges on the thin film, it undergoes multiple reflections and transmissions at the film interfaces. Within the film, the wave experiences successive internal

reflections, giving rise to constructive or destructive interference depending on the optical path difference. Each transmitted and reflected component acquires a phase shift that is determined by the film thickness d, the RI n_1, and the angle of propagation θ_1 inside the layer. The phase shift β is expressed as:

$$\beta = \frac{2\pi}{\lambda} n_1 d \cos\theta_1, \tag{2.15}$$

where λ is the wavelength of the incident light in vacuum.

The reflection (r_{jk}) and transmission (t_{jk}) amplitude coefficients at the interface between medium j and medium k depend on the polarization. For p-polarization (TM) and s-polarization (TE), they are given by the Fresnel formulas:

$$r_{jk}^{(p)} = \frac{n_k \cos\theta_j - n_j \cos\theta_k}{n_k \cos\theta_j + n_j \cos\theta_k}, \quad r_{jk}^{(s)} = \frac{n_j \cos\theta_j - n_k \cos\theta_k}{n_j \cos\theta_j + n_k \cos\theta_k}, \tag{2.16}$$

$$t_{jk}^{(p)} = \frac{2n_j \cos\theta_j}{n_k \cos\theta_j + n_j \cos\theta_k}, \quad t_{jk}^{(s)} = \frac{2n_j \cos\theta_j}{n_j \cos\theta_j + n_k \cos\theta_k}. \tag{2.17}$$

For a single film (medium 1) of thickness d, deposited on a substrate (medium 2) and illuminated from an incident medium (0), the net amplitude reflection coefficient (r_{012}) and transmission coefficient (t_{012}) as observed from medium 0 can be rigorously formulated as the superposition of all multiple internally reflected and transmitted waves within the film [70]:

$$r_{012} = r_{01} + t_{01}t_{10}r_{12}e^{-2i\beta} + t_{01}t_{10}r_{10}r_{12}^2 e^{-4i\beta} + \cdots, \tag{2.18}$$

$$t_{012} = t_{01}t_{12}e^{-i\beta} + t_{01}t_{12}r_{10}r_{12}e^{-3i\beta} + \cdots. \tag{2.19}$$

These relations can be simplified as:

$$r_{012} = \frac{r_{01} + r_{12}e^{-2i\beta}}{1 + r_{01}r_{12}e^{-2i\beta}}, \tag{2.20}$$

$$t_{012} = \frac{t_{01}t_{12}e^{-2i\beta}}{1 + r_{01}r_{12}e^{-2i\beta}}. \tag{2.21}$$

Finally, the reflectance and transmittance (power quantities) follow as:

$$R_{012} = |r_{012}|^2, \qquad T_{012} = \frac{n_2 \cos\theta_2}{n_0 \cos\theta_0} |t_{012}|^2. \tag{2.22}$$

The theoretical framework developed for a single-layer structure can, in principle, be extended to the analysis of multilayer systems. However, as the number of layers increases, the corresponding number of partial waves grows significantly, rendering the computation increasingly complex and difficult to manage. To address this challenge, several methods have been proposed to simplify and optimize the calculation process.

2.4 Simulation methods for one-dimensional photonic crystals

The previously discussed theoretical framework for a single-layer system can, in principle, be extended to the analysis of multilayer PhCs structures. However, as the number of layers increases, the associated subwaves grow exponentially, leading to a rapid escalation in computational complexity and rendering direct calculations increasingly impractical. To address this challenge, several numerical techniques have been developed to simplify and optimize the analysis. Among the most widely employed approaches are the Transfer Matrix Method (TMM), the Finite-Difference Time-Domain (FDTD) method, and the Plane Wave Expansion (PWE) method. These methods provide efficient and reliable tools for modeling the optical response of 1D PhCs under various physical conditions.

2.4.1 Transfer Matrix Method (TMM)

The Transfer Matrix Method (TMM) is a widely used and relatively straightforward analytical technique for investigating the optical properties of one-dimensional layered structures, such as 1D PhCs. It operates by breaking down a multilayer structure into individual layers, each characterized by its own RI and thickness. The electromagnetic fields at the interfaces between these layers are then related using a series of transfer matrices. By multiplying these matrices, one can determine the overall transmission and reflection characteristics of the entire structure. Layered structures can be represented:

The electric field $E(x)$ consists of a right-traveling wave and a left-traveling wave and can be written as

$$E(x) = Re^{-ik_x x} + Le^{ik_x x} \equiv A(x) + B(x), \tag{2.23}$$

Consider a stratified medium consisting of N layers, where the RI of the media are given by the sequence $(n_0, n_1, \ldots, n_N, n_s)$. Let A_i represent the amplitude of the right-propagating wave and B_i represent the amplitude of the left-propagating wave in the electric field for medium i. The thickness of each layer is defined as follows:

$$\begin{cases} d_1 = x_1 - x_0 \\ d_2 = x_2 - x_1 \\ \vdots \\ d_N = x_N - x_{N-1} \end{cases} \tag{2.24}$$

The electric field corresponding to a general plane-wave solution of the wave equation

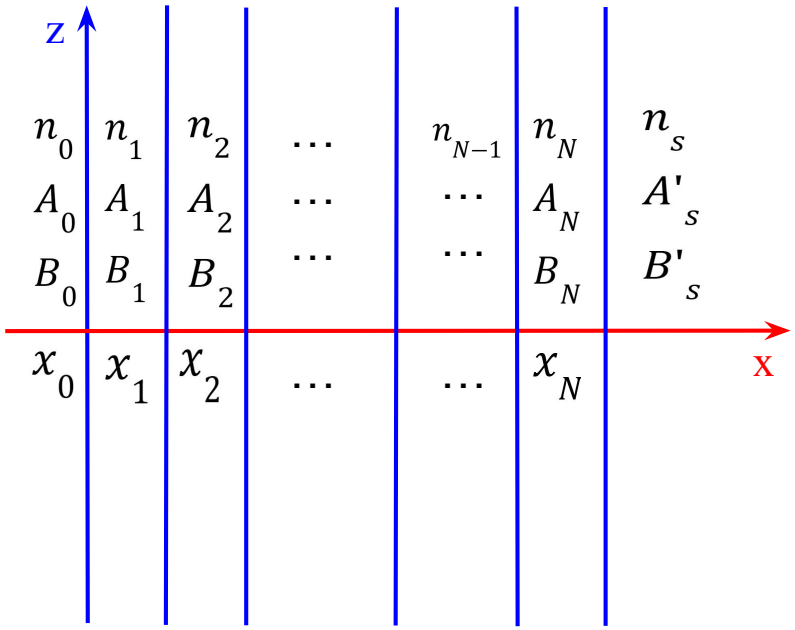

Figure 2.3: Schematic of a multilayer structure.

(Eq. 2.6) can be expressed in the form

$$E = E(x)\, e^{i(\omega t - \beta z)}. \tag{2.25}$$

The spatial distribution of the electric field $E(x)$ within the i-th medium can be written as

$$E(x) = \begin{cases} A_0 e^{-ik_{0x}(x-x_0)} + B_0 e^{ik_{0x}(x-x_0)}, & x < x_0, \\ \vdots & \\ A_l e^{-ik_{lx}(x-x_l)} + B_l e^{ik_{lx}(x-x_l)}, & x_{l-1} < x < x_l, \\ \vdots & \\ A_N e^{-ik_{Nx}(x-x_N)} + B_N e^{ik_{Nx}(x-x_N)}, & x_N < x, \end{cases} \tag{2.26}$$

where k_{lx} denotes the x-component of the wave vector in the l-th medium, which is related to the propagation angle θ_l through

$$k_{lx} = n_l \frac{\omega}{c} \cos\theta_l, \qquad l = 0, 1, 2, \ldots, N, s. \tag{2.27}$$

According to Eqs. (2.26) and (2.23), the coefficients A_l and B_l correspond to the amplitudes of forward- and backward-propagating plane waves at the interface $x = x_l$. Therefore, the field amplitudes can be related through the transfer-matrix formalism

as

$$\begin{pmatrix} A_0 \\ B_0 \end{pmatrix} = D_0^{-1} D_1 \begin{pmatrix} A_1 \\ B_1 \end{pmatrix}, \tag{2.28}$$

and

$$\begin{pmatrix} A_l \\ B_l \end{pmatrix} = P_l D_l^{-1} D_{l+1} \begin{pmatrix} A_{l+1} \\ B_{l+1} \end{pmatrix}, \qquad l = 1, 2, \ldots, N. \tag{2.29}$$

Here, the index $N+1$ refers to the substrate s, with $A_{N+1} = A'_s$ and $B_{N+1} = B'_s$. The explicit form of the matrices D_l and P_l can be defined as follows [70]:

$$D_l = \begin{pmatrix} 1 & 1 \\ n_l \cos\theta_l & -n_l \cos\theta_l \end{pmatrix} \quad \text{for S-wave} \tag{2.30}$$

$$D_l = \begin{pmatrix} \cos\theta_l & \cos\theta_l \\ n_l & -n_l \end{pmatrix} \quad \text{for p-wave} \tag{2.31}$$

which represents the boundary conditions at each interface, and

$$P_l = \begin{pmatrix} e^{i\phi_l} & 0 \\ 0 & e^{-i\phi_l} \end{pmatrix}, \tag{2.32}$$

which describes the phase accumulation within the l-th layer. The phase shift ϕ_l is defined as

$$\phi_l = k_{lx} d_l, \tag{2.33}$$

The relationship between the wave amplitudes in the incident medium (A_0, B_0) and those in the substrate medium (A'_s, B'_s) can be expressed as

$$\begin{pmatrix} A_0 \\ B_0 \end{pmatrix} = \mathbf{M} \begin{pmatrix} A'_s \\ B'_s \end{pmatrix}, \tag{2.34}$$

where $\mathbf{M}$ denotes the total transfer matrix of the multilayer structure. It is defined by

$$\mathbf{M} = \begin{pmatrix} M_{11} & M_{12} \\ M_{21} & M_{22} \end{pmatrix} = D_0^{-1} \left[\prod_{l=1}^{N} \left(D_l P_l D_l^{-1} \right) \right] D_s. \tag{2.35}$$

Here D_l and P_l are the interface and propagation matrices of the l-th layer, respectively, and D_s denotes the matrix of the substrate.

2.4.2 Finite-Difference Time-Domain (FDTD) Method

The Finite-Difference Time-Domain (FDTD) method is a robust numerical technique for analyzing the propagation of electromagnetic waves and their interactions with

matter. The terminology reflects its foundation:

- **Finite Difference:** Spatial and temporal derivatives are approximated by finite differences on a discrete grid.
- **Time Domain:** Maxwell's equations are directly solved in the time domain, capturing the temporal evolution of fields.

The formulation of the method stems from two of Maxwell's curl equations, namely Faraday's and Ampère's laws:

$$\nabla \times \vec{E} = -\mu \frac{\partial \vec{H}}{\partial t}, \tag{2.36}$$

$$\nabla \times \vec{H} = \epsilon \frac{\partial \vec{E}}{\partial t}, \tag{2.37}$$

where $\vec{E}$ and $\vec{H}$ denote the electric and magnetic fields, respectively, while ϵ and μ represent the permittivity and permeability of the medium. In Cartesian coordinates, Eqs. (2.36)–(2.37) expand to the following system:

$$\begin{cases} -\mu \dfrac{\partial H_x}{\partial t} = \dfrac{\partial E_z}{\partial y} - \dfrac{\partial E_y}{\partial z}, \\ -\mu \dfrac{\partial H_y}{\partial t} = \dfrac{\partial E_x}{\partial z} - \dfrac{\partial E_z}{\partial x}, \\ -\mu \dfrac{\partial H_z}{\partial t} = \dfrac{\partial E_y}{\partial x} - \dfrac{\partial E_x}{\partial y}, \\ \varepsilon \dfrac{\partial E_x}{\partial t} = \dfrac{\partial H_z}{\partial y} - \dfrac{\partial H_y}{\partial z}, \\ \varepsilon \dfrac{\partial E_y}{\partial t} = \dfrac{\partial H_x}{\partial z} - \dfrac{\partial H_z}{\partial x}, \\ \varepsilon \dfrac{\partial E_z}{\partial t} = \dfrac{\partial H_y}{\partial x} - \dfrac{\partial H_x}{\partial y}. \end{cases} \tag{2.38}$$

The discretization scheme was pioneered by Yee in 1966, introducing the *Yee lattice* or *Yee grid* [71]. In this scheme, the computational domain is subdivided into cubic cells. The electric field components (E_x, E_y, E_z) are defined along the edges of each cell, while the magnetic field components (H_x, H_y, H_z) are defined on the cell faces, as illustrated in Fig. 2.4.

This staggered arrangement inherently satisfies Maxwell's curl relations and facilitates a consistent discretization of the governing equations. For instance, the time derivative of the electric field is approximated as:

$$\frac{\partial E}{\partial t} \approx \frac{E^{n+1/2} - E^{n-1/2}}{\Delta t}, \tag{2.39}$$

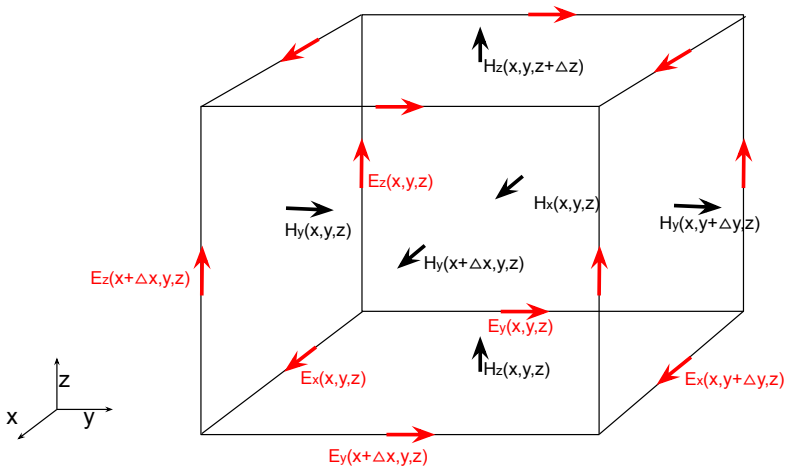

Figure 2.4: Schematic of the Yee cell illustrating the staggered placement of E and H components.

and the spatial derivative as:

$$\frac{\partial E}{\partial x} \approx \frac{E_{i+1/2} - E_{i-1/2}}{\Delta x}. \tag{2.40}$$

As an example, the update equation for the z-component of Faraday's law takes the form [71]:

$$E_z^{n+1}(i,j,k) = E_z^n(i,j,k) + \frac{\Delta t}{\epsilon \Delta x}\Big[H_y^{n+1/2}(i+1/2,j,k) - H_y^{n+1/2}(i-1/2,j,k)\Big]$$

$$-\frac{\Delta t}{\epsilon \Delta y}\Big[H_x^{n+1/2}(i,j+1/2,k) - H_x^{n+1/2}(i,j-1/2,k)\Big]. \tag{2.41}$$

Interpretation: The updated field E^{n+1} depends on its previous value E^n and the curl of the magnetic field components at neighboring nodes.

Algorithmic Procedure:

1. Initialize the spatial grid $(\Delta x, \Delta y, \Delta z)$ and assign material parameters (ϵ, μ).

2. Update the magnetic field using:

$$H^{n+1/2} = H^{n-1/2} + \frac{\Delta t}{\mu}(\nabla \times E^n). \tag{2.42}$$

3. Update the electric field using:

$$E^{n+1} = E^n + \frac{\Delta t}{\epsilon}(\nabla \times H^{n+1/2}). \tag{2.43}$$

4. Apply the source excitation (e.g., Gaussian pulse or harmonic source).

5. Repeat the update cycle for all time steps.

Stability Criterion: To ensure numerical stability, the Courant–Friedrichs–Lewy (CFL) condition must be satisfied [72, 73]:

$$\Delta t \leq \frac{1}{c.\sqrt{\left(\frac{1}{\Delta x}\right)^2 + \left(\frac{1}{\Delta y}\right)^2 + \left(\frac{1}{\Delta z}\right)^2}}, \tag{2.44}$$

where c is the speed of light in free space.

2.4.3 Plane-Wave Expansion (PWE) Method

The Plane-Wave Expansion (PWE) method is an established frequency-domain technique for calculating the photonic band structure $\omega(\mathbf{k})$ of periodic dielectric media[74, 75]. The approach leverages Fourier analysis and Bloch's theorem to reformulate Maxwell's equations as an eigenvalue problem.

According to Bloch's theorem, the electric field in a periodic medium can be expressed as:

$$\mathbf{E}_{\mathbf{k}}(\mathbf{r}) = e^{i\mathbf{k}\cdot\mathbf{r}}\,\mathbf{u}_{\mathbf{k}}(\mathbf{r}), \tag{2.45}$$

where $\mathbf{u}_{\mathbf{k}}(\mathbf{r})$ is periodic with the lattice.

For TE polarization, the wave equation in a periodic medium takes the form:

$$\nabla \times \nabla \times \mathbf{E}(\mathbf{r}) = \frac{\omega^2}{c^2}\epsilon(\mathbf{r})\mathbf{E}(\mathbf{r}), \tag{2.46}$$

where the dielectric function satisfies $\epsilon(z+d) = \epsilon(z)$ with lattice constant d.

The Bloch-Fourier expansion of the field reads:

$$E_x(z) = \sum_{n=-\infty}^{\infty} E_{x,n}\, e^{i(G_n + k_z)z}, \tag{2.47}$$

where $G_n = 2\pi n/d$ is the reciprocal lattice vector.

The inverse dielectric function is similarly expanded as:

$$\frac{1}{\epsilon(z)} = \sum_{m=-\infty}^{\infty} \kappa_m\, e^{iG_m z}, \tag{2.48}$$

with Fourier coefficients:

$$\kappa_m = \frac{1}{d}\int_{-d/2}^{d/2} \frac{1}{\epsilon(z)} e^{-iG_m z}\, dz. \tag{2.49}$$

Substituting Eqs. (2.47)–(2.48) into Eq. (2.46) and applying orthogonality yields a coupled system of algebraic equations for the coefficients $E_{x,n}$.

This leads to the generalized eigenvalue problem:

$$\sum_n (\mathbf{G}_n + \mathbf{k})\, \kappa_{p-n}\, E_{x,n} = \frac{\omega^2}{c^2} E_{x,p}, \tag{2.50}$$

or equivalently in matrix notation:

$$\hat{M}(\mathbf{k})\, \mathbf{E} = \frac{\omega^2}{c^2}\, \mathbf{E}. \tag{2.51}$$

Band Structure Computation: For each Bloch wavevector k_z in the first Brillouin zone:

1. Construct the operator $\hat{M}(k_z)$.
2. Solve the eigenvalue problem to obtain $\lambda_i = \omega_i^2/c^2$.
3. Extract the photonic band frequencies as $\omega_i = c\sqrt{\lambda_i}$.

Chapter 3

Design of a One-Dimensional Photonic Crystal Biosensor

3.1 Introduction

This chapter develops a compact transfer-matrix-based framework for designing a one-dimensional photonic crystal (1D PhC) biosensor comprising alternating dielectric layers and a central defect cavity that hosts the analyte. The global transfer matrices of the periodic and defect-bearing stacks were formulated to obtain transmission and reflection spectra under lossless conditions, ensuring energy conservation. The performance metrics central to biosensing, namely, sensitivity, quality factor, figure of merit, and signal-to-noise ratio, are defined to connect resonance features to RI perturbations. Material dispersion and index contrast are explicitly treated via SiO_2/TiO_2, a pair that yields a wide bandgap and strong field confinement. Enforcing the quarter-wave condition positions the bandgap at the target wavelength. Illustrative calculations guide the choice of $\lambda_c = 800$ nm as a practical operating point.

3.2 Theoretical Formulation

3.2.1 Global Transfer Matrix

Electromagnetic propagation in 1D PhCs can be efficiently studied by means of the Transfer Matrix Method (TMM), which has already been introduced in Chapter 2, see Subsection 2.4.1.

In this section, we define the product of two matrix structures:

- The first corresponds to a simple 1D PhCs composed of two alternating dielectric layers.

- The second corresponds to a 1D PhCs with two alternating layers and a central defect inserted in the middle of the stack.

For the defect-free case, the global transfer matrix of N bilayers is expressed as

$$M_{\mathrm{PC}} = D_{in}^{-1} \left(m_1 m_2\right)^N D_{out}. \tag{3.1}$$

where $m_i = D_i^{-1} P_i D_i$ and M_1 and M_2 represent the transfer matrices of the two materials.

When a defect cavity is introduced at the center of the multilayer stack, the global transfer matrix becomes

$$M_{\mathrm{tot}} = D_{in}^{-1} \left(m_1 m_2\right)^N m_3 \left(m_1 m_2\right)^N D_{out}, \tag{3.2}$$

where m_3 denotes the transfer matrix of the defect layer.

3.2.2 Transmittance and Reflectance Spectra

The spectral characteristics of a 1D PhC are typically described by its transmittance and reflectance. These parameters provide direct insight into the optical response of the multilayer system and are essential for biosensing applications. Within the Transfer Matrix Method (TMM), the global transfer matrix M_{tot} relates the incident, reflected, and transmitted field amplitudes.

Transmittance. Once M_{tot} is obtained, the transmission coefficient t can be written as

$$t = \frac{1}{M_{11}}, \tag{3.3}$$

where M_{11} is the $(1,1)$ element of the global transfer matrix. The power transmittance is then calculated as

$$T(\lambda) = \frac{n_{\mathrm{out}} \cos\theta_{\mathrm{out}}}{n_{\mathrm{in}} \cos\theta_{\mathrm{in}}} \left| \frac{1}{M_{11}} \right|^2, \tag{3.4}$$

where n_{in} and n_{out} denote the RI of the input and output media, respectively, while θ_{in} and θ_{out} are the corresponding incidence and transmission angles.

Reflectance. Similarly, the reflection coefficient r of the multilayer structure is obtained from the transfer matrix as

$$r = \frac{M_{21}}{M_{11}}, \tag{3.5}$$

where M_{21} is the $(2,1)$ element of M_{tot}. The reflectance R is then expressed as

$$R(\lambda) = |r|^2 = \left|\frac{M_{21}}{M_{11}}\right|^2. \tag{3.6}$$

Energy conservation. For a lossless PhC composed of dielectric layers, the relation

$$T(\lambda) + R(\lambda) = 1 \tag{3.7}$$

holds, ensuring that all incident light is either transmitted or reflected. This property allows both spectra to be used for characterizing the photonic bandgap (PBG) and the defect modes.

3.2.3 Performance Parameters of the Biosensor

To fully evaluate the performance of the proposed biosensor, several key parameters are introduced. These include the sensitivity (S),Quality factor (Q), signal-to-noise ratio (SNR), and figure of merit (FoM). They provide quantitative measures of the device's capability to detect small variations in the RI of the analyte.

Sensitivity: The sensitivity (S) of the biosensor is defined as the shift in the resonance wavelength ($\Delta\lambda_{\text{res}}$) with respect to the change in the RI (Δn) of the sensing medium, and it can be expressed as [76]:

$$S = \frac{\Delta\lambda_{\text{res}}}{\Delta n} \quad [\text{nm/RIU}] \tag{3.8}$$

Quality Factor: The quality factor (Q) is a measure of the sharpness of the resonance peak, defined as the ratio between the resonance wavelength (λ_{res}) and the full width at half maximum (FWHM) [76]:

$$Q = \frac{\lambda_{\text{res}}}{\text{FWHM}} \tag{3.9}$$

Figure of Merit: The figure of merit (FoM) is another critical performance indicator, defined as the ratio between S and FWHM of the resonance curve [77]:

$$\text{FoM} = \frac{S}{\text{FWHM}} \quad [\text{RIU}^{-1}] \tag{3.10}$$

Signal to Noise Ratio: The signal-to-noise ratio (SNR) is defined as the ratio of the resonance peak wavelength shift ($\Delta\lambda_{\text{res}}$) to the spectral $FWHM$. It is expressed as [77]:

$$SNR = \frac{\Delta\lambda_{\text{res}}}{FWHM} \tag{3.11}$$

These parameters serve as standard benchmarks for comparing biosensor designs. A high S, Q and FoM, combined with a SNR, indicate strong performance in detecting small variations of the analyte's RI.

3.3 Structural Design

3.3.1 General Structure

The basic design of the biosensor consists of a 1D PhC formed by alternating layers of two dielectric materials with different RI, arranged to create a multilayer stack. The general structure can be written as

$$(n_1 n_2)^N \; C \; (n_1 n_2)^N, \tag{3.12}$$

where n_1 and n_2 are the RI of the two chosen materials, N is the number of bilayers on each side, and C denotes a central defect cavity. This cavity, with thickness d_0, breaks the periodicity and can be filled with the analyte under investigation (e.g., blood components). The defect cavity acts as a resonant site, producing localized optical modes inside PBG.

3.3.2 Choice of Materials

Silicon dioxide (SiO_2) and titanium dioxide (TiO_2) were chosen as the constituent materials of the designed biosensor. SiO_2 is a low-index dielectric with high optical transparency and low absorption in the visible and near-infrared regions, making it suitable for forming the low-index layers. TiO_2, on the other hand, provides a much higher RI and strong dispersion, ensuring effective light confinement and the formation of a wide PBG.

The high RI contrast between the two materials ($\Delta n \approx 0.8$) is the key factor in achieving a pronounced bandgap, which enhances the S of the PhC biosensor.

The RI of SiO_2 and TiO_2 are given in arrangement [78]:

$$n_1^2(\lambda) = 1 + \frac{0.6961663\,\lambda^2}{\lambda^2 - 68404.3} + \frac{0.4079426\,\lambda^2}{\lambda^2 - 116241.42} + \frac{0.8974794\,\lambda^2}{\lambda^2 - 9896161.2}, \tag{3.13}$$

$$n_2^2(\lambda) = 5.913 + \frac{244100}{\lambda^2 - 80300}. \tag{3.14}$$

3.3.3 Layer Thickness: Quarter-wave Condition

The thicknesses of the alternating layers are chosen according to the quarter-wave condition to center the PBG at the design wavelength. This condition reads

$$n_1 d_1 \;=\; n_2 d_2 \;=\; \frac{\lambda_c}{4}, \tag{3.15}$$

where n_1 and n_2 are the RI of the two materials, d_1 and d_2 are their physical thicknesses, and λ_c is the central (design) wavelength.

By satisfying (3.15), the periodic stack produces a PBG centered near λ_c. The spectral response can then be tuned by adjusting N and the defect cavity thickness d_0, which respectively influence the bandgap sharpness.

We will apply the quarter-wavelength law to a simple 1D PhC by calculating the transmittance spectrum (3.4) for the matrix (3.1) at different central wavelengths $\lambda_c =$ (400, 600, 800, and 1000 nm) in the visible and infrared range.

Table 3.1: Calculated layer thicknesses and PBG values for different central wavelengths λ_c.

λ_c (nm)	d_{SiO_2} (nm)	d_{TiO_2} (nm)	PBG (nm)
400	68.02	33.38	148.79
600	102.88	57.58	241.46
800	137.62	79.37	323.94
1000	172.36	100.58	405.55

The table 3.1 summarizes the calculated quarter-wave thicknesses of SiO_2 and TiO_2 layers together with the corresponding PBG values for various design wavelengths.

The figure 3.1 illustrates how the quarter-wave design shifts the central position of the PBG, with higher design wavelengths leading to a red-shift in the transmission spectrum.

3.3.4 Sensor Design

After calculating the PBG values for different central wavelengths λ_c, the initial design wavelength was selected as $\lambda_c = 800$ nm in order to analyze blood components within the visible spectral region and to obtain a wide photonic band gap. In this spectral range, the high refractive-index contrast between SiO_2 and TiO_2 provides strong optical confinement and well-defined defect resonances suitable for biosensing applications.

According to the quarter-wave condition, the corresponding layer thicknesses are $d_1 = 138$ nm for SiO_2 and $d_2 = 79$ nm for TiO_2. The defect layer thickness, denoted by d_0, is defined as an integer multiple of the lattice period D, where $D = d_1 + d_2$ represents the total thickness of one unit cell composed of SiO_2 and TiO_2 layers in the 1D PhC structure. This configuration ensures that the defect mode is positioned close

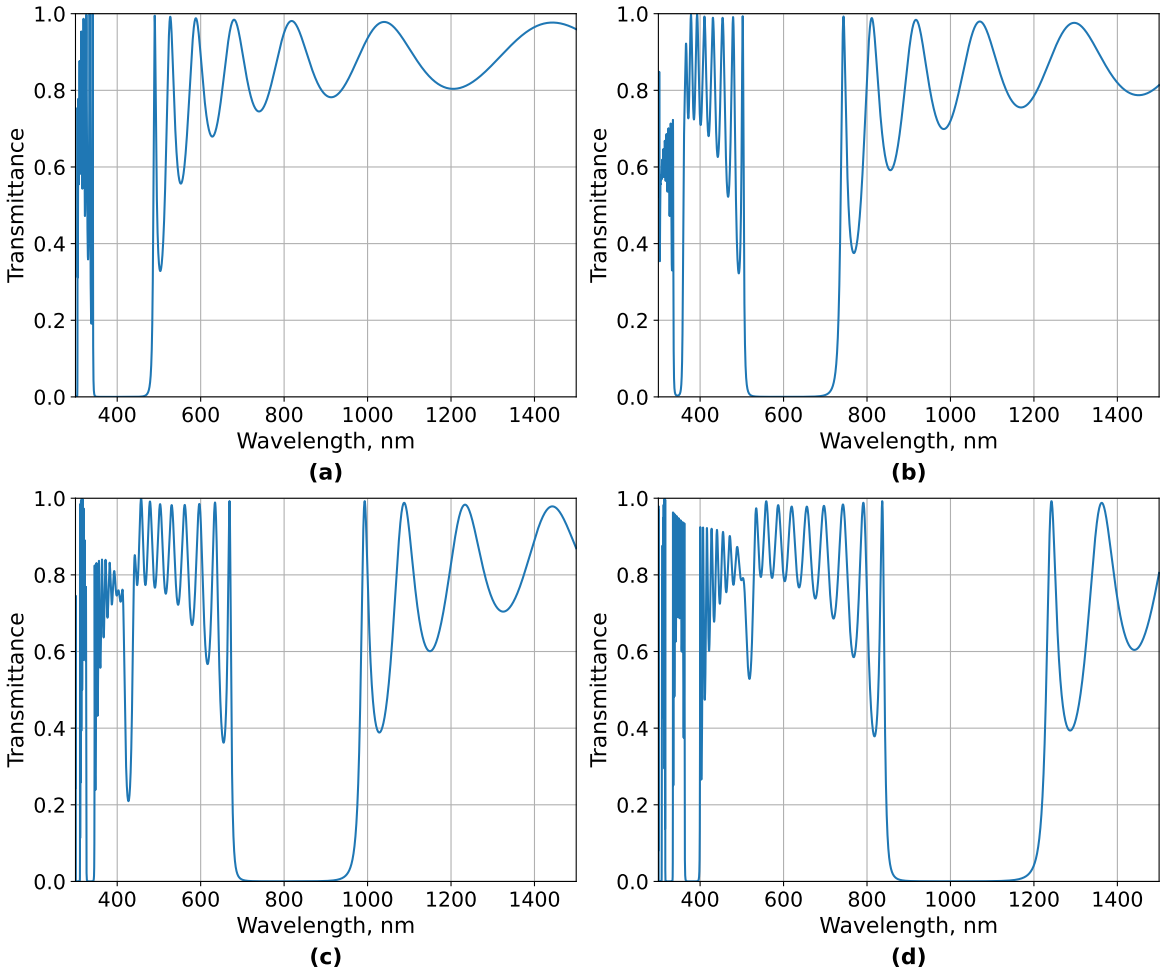

Figure 3.1: Transmission spectra of 1D PhCs under the quarter-wave condition for different central wavelengths λ_c: (a) 400 nm, (b) 600 nm, (c) 800 nm, and (d) 1000 nm.

to the central design wavelength, thereby maximizing the sensitivity (S) for biosensing applications.

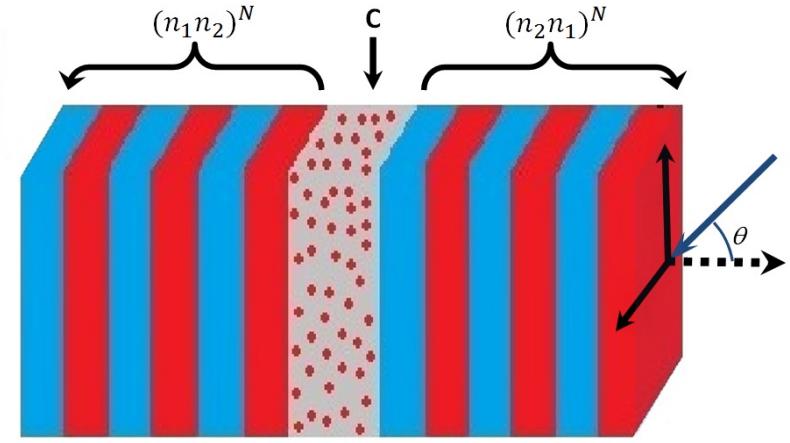

Figure 3.2: Illustration of the designed 1D PhCs

3.4 Conclusion

A rigorous yet parsimonious TMM formulation has been presented for 1D PhC biosensors with a central defect, enabling direct computation of spectral coefficients and verification of energy conservation. The SiO_2/TiO_2 platform, combined with quarter-wave thicknesses, produces a pronounced PBG and a narrow defect resonance whose position and linewidth encode analyte RI. The adopted performance metrics (S, Q, FoM, and SNR) provide a consistent basis for comparing designs and optimising the number of bilayers and cavity thickness. The selected $\lambda_c = 800$ nm serves as a well-justified starting point for parametric refinement, including dispersion-aware S analysis and tolerance to fabrication-induced variations and loss.

Chapter 4

Results and Analysis of the 1D Photonic Crystal Biosensor

4.1 Introduction

The examination of human blood constituents is pivotal in clinical diagnostics, as minor fluctuations in plasma, erythrocytes, leukocytes, or hemoglobin levels might act as preliminary markers of disease states. Traditional biochemical assays, while precise and dependable, tend to be laborious and expensive, prompting the pursuit of swift and economical optical biosensing alternatives. Photonic crystal (PhC) structures have emerged as formidable contenders for manipulating light propagation via photonic band gaps (PBGs).

One-dimensional photonic crystals (1D PhCs) are notably appealing due to their straightforward production, cost-effectiveness, and heightened sensitivity to refractive index fluctuations. Prior research has established their utility in gas detection [79], temperature measurement [80], and pressure assessment [81]. This study examines the transmittance spectrum of a defective 1D PhC biosensor, consisting of alternating SiO_2/TiO_2 multilayers, for the real-time detection of human blood components within the visible wavelength range. The transfer matrix method (TMM), executed in Python, was employed to model and analyze the optical response of the sensor.

The suggested biosensor has the ability to identify alterations in the transmittance profile related to four specific blood components—plasma, white blood cells, hemoglobin, and red blood cells—within the PBG. A parametric analysis was performed by altering the defect layer thickness (d_0), the number of periodic layers (N), and the incidence angle (θ_i) to enhance the sensitivity and performance of the sensor.

4.2 Composition and Functions of Human Blood-Components

The composition of human blood provides critical information about an individual's physiological state, as it reflects the functional balance of tissues and organs throughout the body. Even slight deviations from the normal concentration ratios or properties of blood components may disrupt homeostasis and negatively affect overall health [82, 83].

Human blood is primarily composed of three major cellular elements:

- Red blood cells (RBCs), which play a vital role in the transport of oxygen from the lungs to body tissues and the return transport of carbon dioxide for exhalation.
- White blood cells (WBCs), which serve as a key component of the immune system, protecting the body against infections and foreign agents.
- Platelets, which are responsible for initiating clot formation, thereby preventing excessive bleeding and contributing to wound healing processes [84–86].

These cellular components are suspended in plasma, the liquid portion of blood, which serves as a carrier for nutrients, metabolic waste, proteins, hormones, and antibodies. The proper regulation of each blood component is essential for maintaining physiological stability and ensuring the body's overall health and functionality[87, 88].

4.3 Influence of Structural Parameters

The performance of the proposed 1D PhC biosensor is strongly dependent on its structural parameters. A parametric analysis was carried out to examine the influence of three key factors: the defect layer thickness d_0, the number of periodic layers N , and the incidence angle θ. In the designed structure (Figure 3.2), the blood sample is introduced into the central cavity C of thickness d_0. The refractive indices (RI) of the selected blood components are adopted from previously reported values in the literature [89]: blood plasma $n_{\mathrm{bp}} = 1.35$, white blood cells $n_{\mathrm{wb}} = 1.36$, hemoglobin $n_{\mathrm{hb}} = 1.38$, and red blood cells $n_{\mathrm{rb}} = 1.40$. These values correspond to experimental measurements performed at room temperature ($T = +24\,^{\circ}\mathrm{C}$) over the spectral range of 480–1550 nm using a multi-wavelength Abbe refractometer [90].

4.3.1 Defect Layer Thickness

We examined how the thickness d_0 of the defect layer affects the sensor by conducting simulations of the transmittance spectrum across a range of d_0 values, as shown in Figure 4.1. The transmittance spectrum was analyzed at $d_0 = (2D, 3D, 4D, 5D, 6D, 8D, 9D, 10D)$.

These simulations were conducted with a periodic number of layers N = 5 and a incidence angle θ_i. From these simulations, we extracted the PBG, wavelength associated with the resonant peak (λ_{res}) within the PBG, and full width at half maximum (FWHM) of the peaks, as detailed in Table 4.1. Subsequently, the sensor parameters were derived from these results table 4.2.

Table 4.1: Simulation results of cavity d_0 for different indices and defect thicknesses.

Index	1.35	1.36	1.38	1.40	1.35	1.36	1.38	1.40
	4D				6D			
λ_{res} (nm)	718.16	721.04	726.89	732.83	786.77	790.79	798.85	806.93
FWHM	1.26	1.21	1.11	1.04	0.65	0.65	0.67	0.69
λ_{res} (nm)	875.33	879.07	886.49	893.23	925.28	929.49	937.75	945.78
FWHM	1.62	1.70	1.85	2.05	2.68	2.88	3.34	3.88
PBG	384.67	385.31	386.36	387.11	399.41	400.30	401.60	402.29
	9D				10D			
λ_{res} (nm)	723.91	727.86	735.83	743.87	711.31	715.21	723.11	731.10
FWHM	0.68	0.65	0.58	0.54	0.78	0.72	0.63	0.56
λ_{res} (nm)	808.52	813.14	822.38	831.61	785.00	789.58	798.76	807.94
FWHM	0.51	0.52	0.56	0.59	0.44	0.45	0.54	0.61
λ_{res} (nm)	913.89	918.75	928.34	937.74	876.95	881.95	891.92	901.74
FWHM	1.68	1.82	2.15	2.55	0.89	0.94	1.09	1.22
PBG	427.38	427.54	427.70	427.60	415.93	416.90	418.17	418.59

Figure 4.1. Increasing the defect-layer thickness d_0 systematically increases the number of defect modes inside the PBG. Panels (a)–(h) correspond to d_0 = 2D, 3D, 4D, 5D, 6D, 8D, 9D,10D, respectively. For small cavities ($d_0 = 2D$) a single, well-isolated resonance is observed for each analyte (n_c = 1.33–1.40). As d_0 grows ($4D, 6D$), additional resonances emerge, indicating the excitation of higherorder cavity modes. At $d_0 = 10D$ as many as five narrow resonances appear within the PBG; their reduced linewidths imply higher quality factors, but the increased mode density leads to peak crowding and complicates reliable peak identification for sensing. This behavior is consistent with prior reports showing that a thicker defect layer—via a longer optical path and stronger interaction with the Bragg stack—yields more complex transmittance spectra [91, 92]. In view of this trade-off between Q-enhancement and mode crowding, we did not pursue $d_0 > 10D$.

The results presented in Tables (4.1, 4.2) provide a comprehensive analysis of the optical response of 1D PhCS cavities with different defect layer thicknesses (d_0) and RI. From Table 4.1, it is observed that the resonant wavelengths (λ_{res}) shift toward higher values as the refractive index increases, indicating a strong dependence of the cavity

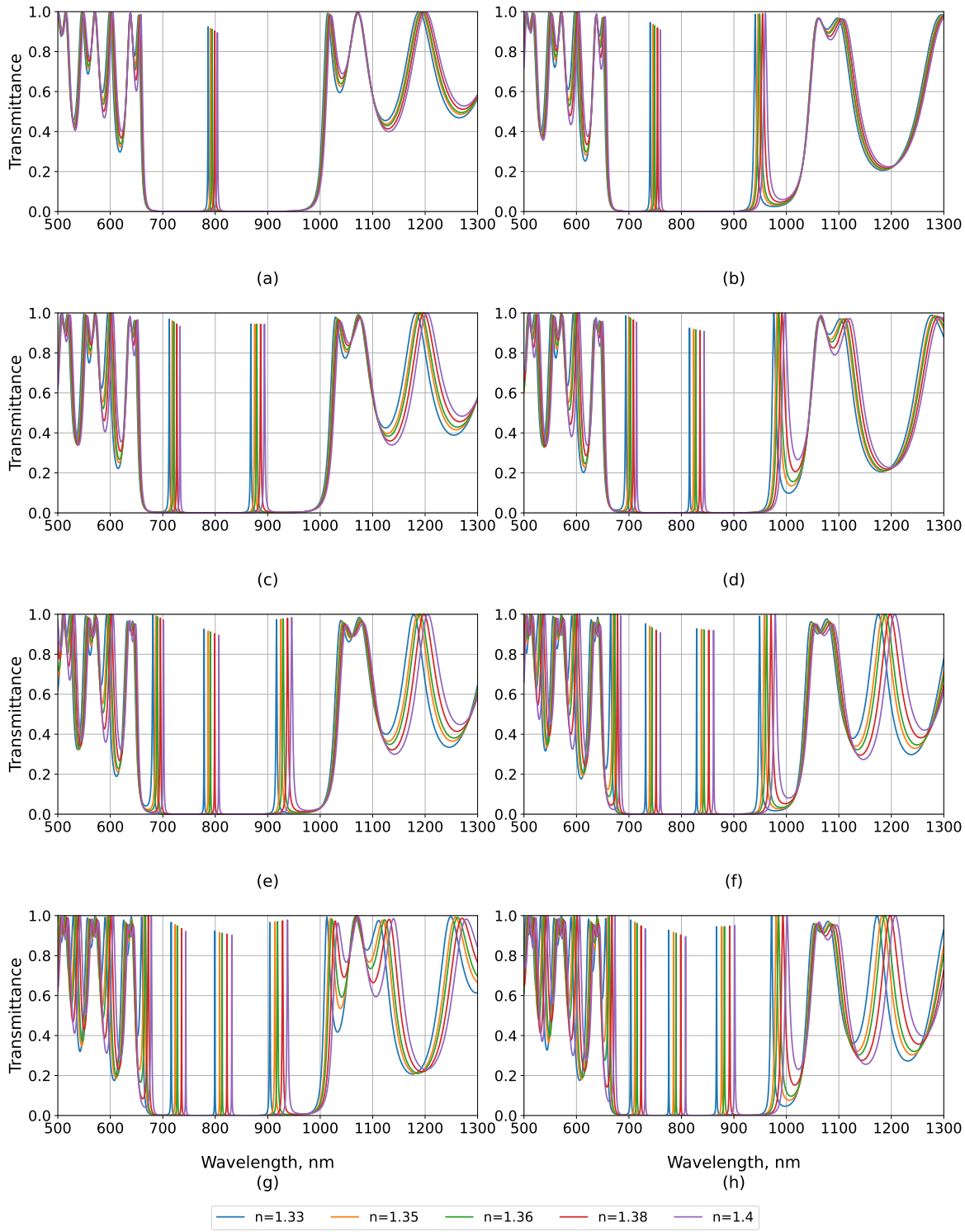

Figure 4.1: Transmittance spectra of the cavity at different defect thicknesses d_0: (a) 2D, (b) 3D, (c) 4D, (d) 5D, (e) 6D, (f) 8D, (g) 9D, and (h) 10D

modes on the surrounding medium. The FWHM generally decreases with increasing index for certain defect thicknesses, implying sharper resonances and potentially higher sensitivity. Furthermore, the PBG values remain relatively stable with only slight variations, reflecting the robustness of the periodic multilayer structure against small

Table 4.2: Performance parameters (S, SNR, Q, FoM) of the cavity at different defect thicknesses d_0.

Index	1.35	1.36	1.38	1.40	1.35	1.36	1.38	1.40
	4D				6D			
S	284.5	285.67	288.4	290.86	401	401.33	402	402.57
SNR	4.52	7.08	12.99	19.58	12.34	18.52	30	40.84
Q	569.97	595.9	654.86	704.64	1210.42	1216.6	1192.31	1169.46
FoM	225.79	236.09	259.87	289.67	616.92	617.44	600	583.42
S	376.5	375.67	378.3	371.86	428	425.67	420.6	415.14
SNR	4.65	6.63	10.2	13.41	9.67	11.2	17	7.49
Q	540.33	517.1	479.18	436.01	345.25	322.74	280.76	243.76
FoM	232.41	220.98	202.05	181.39	159.7	147.80	125.93	107
	9D				10D			
S	391.5	392.67	395	397.39	385	386.67	390	392.71
SNR	11.51	18.12	24.93	31.56	16.11	30.95	49.09	70.48
Q	1064.57	1119.78	1268.67	1377.53	911.93	993.35	1147.79	1305.54
FoM	575.74	604.10	681.03	735.19	493.59	537.04	619.05	701.28
S	461	461.33	461.6	461.67	457	457.8	458	458.14
SNR	18.08	26.61	41.21	54.76	20.75	31.16	50.87	68.23
Q	1583.52	1536.73	1426.67	1298.52	1037.7	1046.8	1127.7	1217.77
FoM	903.92	887.18	824.29	782.32	807.13	803.87	1007.32	974.27
S	492	490	488.67	487.39	522	503.5	502	497.86
SNR	8.08	13.29	19.21	25.07	17.74	27.29	41.77	58.69
Q	543.98	504.81	431.79	367.17	798.54	934.88	981.22	771.45
FoM	292.86	269.23	225.95	188.74	565.17	534.04	458.72	398.29

index changes.

In Table 4.2, the sensitivity (S) increases with defect thickness and higher refractive index, demonstrating that thicker cavities enhance the shift of resonance with respect to index variations. The signal-to-noise ratio (SNR) shows significant improvement for higher d_0, particularly at $9D$ and $10D$, where values exceed 50 for n = 1.40, confirming better detection capability. The quality factor (Q) reaches maximum values above 1700 for the 10D cavity, indicating stronger field confinement and narrower resonance linewidths. Consequently, the figure of merit (FoM) also achieves its highest values for thicker defect layers, especially at $9D$ and $10D$, where it surpasses 900, highlighting the optimized trade-off between sensitivity and spectral selectivity.

Overall, the comparison of both tables (4.1,4.2) suggests that increasing the defect layer thickness enhances the sensing performance of the cavity by simultaneously im-

proving S, SNR, Q, and FoM. However, a balance must be maintained, as excessively high d_0 may lead to practical fabrication challenges and increased insertion losses. These findings underline the critical role of structural parameters in designing high-performance 1D PhC biosensors.

4.3.2 Number of Layers

In this section, we examine how the number of Layers (N) influences the optical response of the biosensor by computing the normal-incidence transmittance spectra for $N \in \{3, 5, 7\}$. Throughout this analysis, the defect layer thickness was held constant at $d_0 = 2D$, and the angle of incidence was fixed at $\theta_i = 0°$. The resulting spectra are shown in Figure 4.2. From the simulated transmittance spectra, we extracted the resonance wavelengths λ_{res}, FWHM, and PBG for each value of N (Table 4.3). In addition, the key performance indicators, S, SNR, Q, and FoM, were evaluated to quantify the sensing performance (Table 4.4).

Table 4.3: Extracted optical parameters (λ_{res}, FWHM, and PBG) for different values of N.

N	RI	λ_{res}	FWHM	PBG
3	1.35	791.22	11.69	442.45
	1.36	793.83	11.78	443.31
	1.38	799.07	11.98	444.94
	1.40	804.34	12.19	446.39
5	1.35	791.59	1.23	361.54
	1.36	794.08	1.23	361.93
	1.38	799.10	1.25	362.61
	1.40	804.13	1.28	363.16
7	1.35	791.63	0.13	327.36
	1.36	794.11	0.12	327.58
	1.38	799.10	0.13	327.95
	1.40	804.11	0.14	328.20

Figure 4.2 highlights the pronounced impact of the bilayer number N on the cavity's spectral response under normal incidence ($\theta_i = 0°$) with a fixed defect thickness $d_0 = 2D$. For a small stack (N = 3), the transmission resonances are comparatively broad (FWHM $\approx$ 12 nm), which is indicative of limited electromagnetic confinement and modest mirror reflectivity. Increasing the stack to N = 5 yields markedly narrower and better isolated resonances (FWHM $\approx$ 1.2 nm), consistent with stronger Bragg reflectivity and enhanced field localization within the defect layer. At N = 7, the

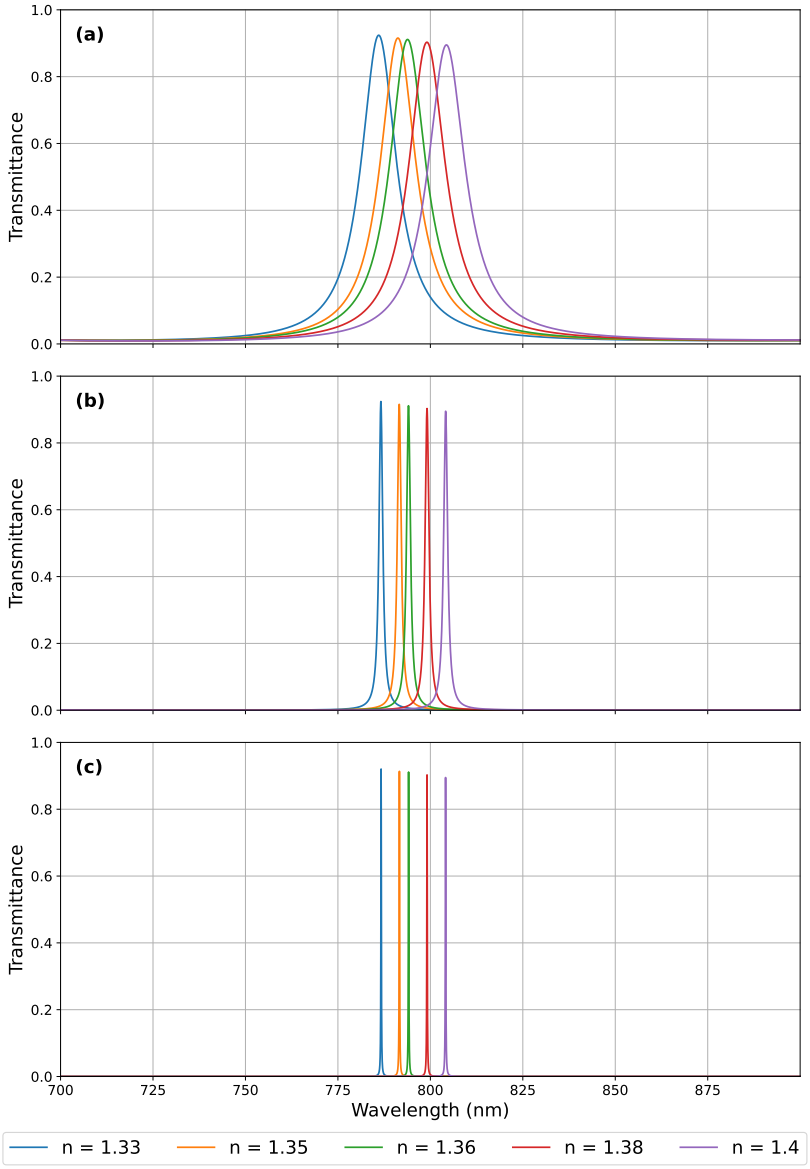

Figure 4.2: Variation in transmittance spectra for different N: (a) N = 3, (b) N = 5, (c) N = 7, (d) N = 9, and (e) N = 11.

resonances become exceptionally sharp, with FWHM approaching 0.14 nm, evidencing high spectral selectivity and fine wavelength discrimination.

Table 4.4: Calculated performance parameters (S, SNR, Q, and FoM) for different values of N.

N	RI	S	SNR	Q	FoM
3	1.35	259.5	0.44	67.68	22.20
	1.36	260.0	0.66	67.39	22.07
	1.38	260.8	1.09	66.70	21.77
	1.40	261.57	1.50	65.98	21.46
5	1.35	248.50	4.04	643.57	202.03
	1.36	248.67	6.07	645.59	202.17
	1.38	249.60	9.98	639.28	199.68
	1.40	250.14	13.68	628.23	195.42
7	1.35	247.50	38.08	6089.46	1903.85
	1.36	247.67	61.92	6617.58	2063.89
	1.38	248.40	95.54	6146.92	1910.77
	1.40	249.00	124.50	5743.64	1778.57

The resonance wavelength λ_{res} systematically redshifts with increasing analyte index (1.35–1.40) for all N , while remaining nearly invariant across N itself (variation $\lesssim$ 3 nm); this confirms that the resonance position is primarily governed by the defectlayer thickness d_0 rather than the mirror length. In contrast, the surrounding photonic bandgap (PBG) width decreases as N grows (from $\sim$ 442 nm to 446 nm at $N = 3$ to $\sim$327 nm to 328 nm at $N = 7$), reflecting a progressively more selective stopband centered around the defect mode (Table 4.3).

Performance metrics consolidate these trends (Tables 4.3 and 4.4). S Sremains largely constant across N ($\sim$ 248–261 nm/RIU), indicating that improvements in detection capability stem from linewidth reduction rather than increased dispersive shift. Consequently, the values of Q and SNR escalate dramatically with N : Q rises from $\sim$ 66 (N = 3) to $\sim$ 640 (N = 5) and reaches $\sim 6 \times 10^3$ at N = 7, while SNR increases by over two orders of magnitude across the same range. The FoM mirrors this behavior, improving from $\sim$ 22 (N = 3) to $\sim$ 200 (N = 5) and up to $\sim 1.8 \times 10^3$ to 2.1×10^3 (N = 7).

In short, increasing (N) doesn't change (λ_{res}) much, but it does make the resonance sharper, which improves spectral resolution and sensing performance. This result is in line with what other studies have found [93, 94]. (N = 7) has the highest accuracy from a design point of view, and (N = 5) strikes a good balance between how hard it is to make and how accurate it is.

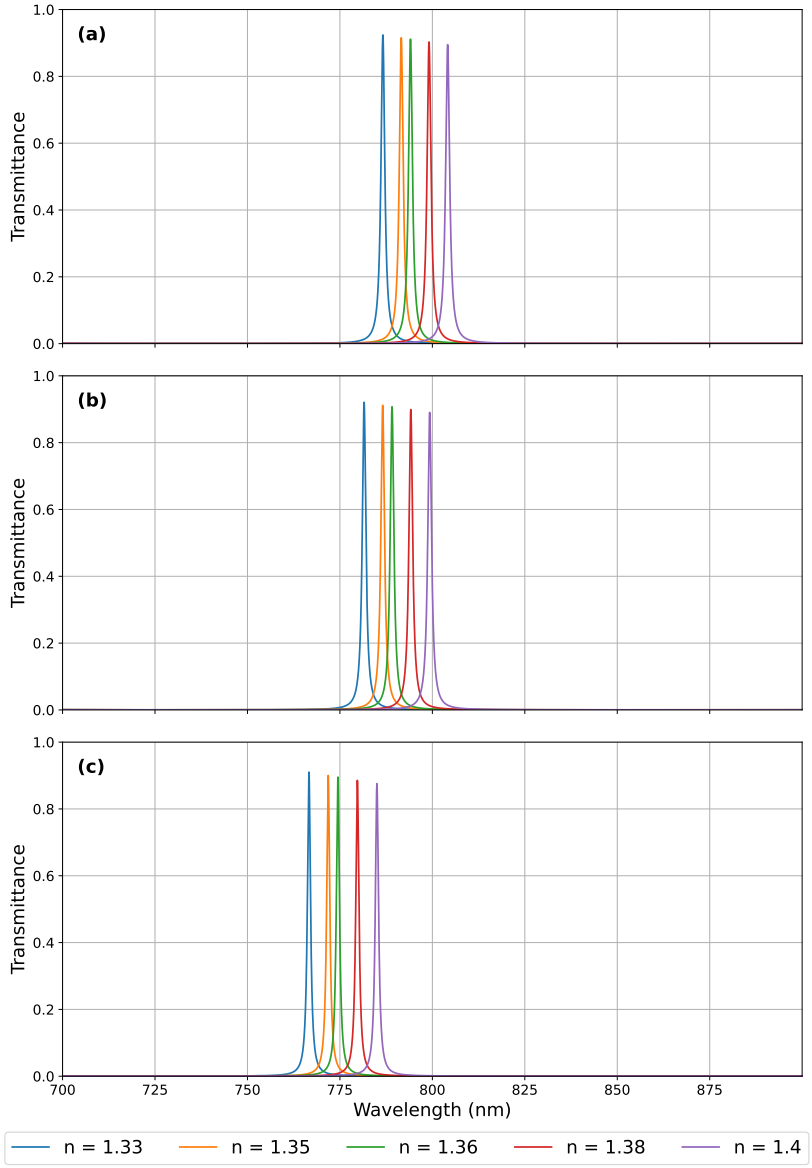

Figure 4.3: Transmittance spectra of the defect resonance for $\theta = 0°, 10°, 20°$ with N = 5 and $d_0 = 2D$.

4.3.3 Incidence Angle

In this section, we assess how the incidence angle θ alters the optical response of the biosensor for a fixed defect thickness $d_0 = 2D$ and a bilayer count N = 5. We computed the normal-to-oblique transmittance spectra for $\theta \in \{0°, 10°, 20°\}$ while sweeping the analyte refractive index from 1.35 to 1.40. The resulting spectra are shown in Figure 4.1.

From the spectra, the defect-mode wavelength λ_{res} exhibits a systematic blue shiftas θ increases, consistent with the reduced effective optical path length at oblique incidence. At fixed θ, λ_{res} retains its expected red shift with increasing analyte index (1.35–1.40). Quantitatively, at n = 1.35 the resonance moves from $\sim 791.6nm$ at 0°to

Table 4.5: Extracted optical parameters (λ_{res}, FWHM, and PBG) for $\theta \in \{0°, 10°, 20°\}$ at $N = 5$ and $d_0 = 2D$.

θ	Index	λ_{res}	FWHM	PBG
0°	1.35	791.59	1.23	361.54
	1.36	794.08	1.23	361.93
	1.38	799.10	1.25	362.61
	1.40	804.13	1.28	363.16
10°	1.35	781.54	1.16	360.32
	1.36	786.57	1.16	361.28
	1.38	789.09	1.17	361.70
	1.40	794.17	1.19	362.43
20°	1.35	766.63	1.00	359.35
	1.36	771.84	1.00	360.48
	1.38	774.46	1.01	360.98
	1.40	779.72	1.02	361.87

$\sim 766.6nm$ at 20°, illustrating the angle-induced spectral compression (Table 4.5).

The linewidth modestly narrows with angle: the FWHM decreases from ~ 1.23 nm at 0° to $\sim$ 1.00–1.02 nm at 20°. The PBG remains nearly unchanged across angles (about 360–362 nm), indicating that obliquity chiefly perturbs the localized defect mode rather than the overall stopband (Table 4.5).

Performance metrics corroborate these trends (Table 4.6). S increases slightly with angle (from $\sim$ 248–250 to $\sim$ 260–263 nm/RIU), while both the values Q and SNR rise due to the narrower resonance at larger θ. Consequently, the FoM improves across the index range when moving from 0° to 20°. In summary, oblique incidence (10°–20°) provides a practical route to sharpen the defect resonance and enhance sensing figures of merit without modifying the stack geometry, at the expense of a predictable angle-dependent blue shift that should be accounted for in calibration.

4.3.4 summary

The combined parametric study highlights that:

- Increasing the defect thickness d_0 introduces multiple resonances and enhances S but complicates the spectrum.
- Increasing N improves resolution and Q, with N = 7 providing optimal results.
- Adjusting the incidence angle θ_i shifts the resonance peaks and offers tunability, though care must be taken to avoid excessive angular dependence.

Table 4.6: Calculated performance parameters (S, SNR, Q, and FoM) for $\theta \in \{0°, 10°, 20°\}$ at $N = 5$ and $d_0 = 2D$.

θ (deg)	Index	S	SNR	Q	FoM
0°	1.35	248.50	4.04	643.57	202.03
	1.36	248.67	6.07	645.59	202.17
	1.38	249.60	9.98	639.28	199.68
	1.40	250.14	13.68	628.23	195.42
10°	1.35	251.50	4.34	678.08	216.81
	1.36	251.67	6.45	674.44	215.10
	1.38	252.60	10.61	667.37	212.27
	1.40	253.29	14.53	655.14	207.61
20°	1.35	260.51	5.21	771.84	260.50
	1.36	261.00	7.75	766.79	258.42
	1.38	261.80	12.83	764.43	256.67
	1.40	262.57	17.67	754.82	252.47

Altogether, the optimized design with $d_0 = 10D$, N = 7, and $\Theta_i = 20°$ exhibited the most favorable performance, combining high S, narrow resonance peaks, and strong robustness for biosensing applications.

4.4 Detection of Hemoglobin Variations

To assess clinical relevance, we optimized the sensor at $N = 7$, $\Theta_i = 20°$, and $d_0 = 10D$, and examined how changes in hemoglobin concentration (C_{HB}) affect the resonant transmittance. The dependence of the sample refractive index n on C_{HB} follows the relation in [76].

Figure 4.4 shows a clear, monotonic red shift of the resonance as n increases (i.e., with increasing C_{HB}) over the 760–800 nm window. Across the tested range (Cells E $\rightarrow$ A, 15.99–30.90 g/dL), the resonance wavelength shifts from 771.57 nm to 789.19 nm, a total excursion of $\sim$ 17.6 nm, confirming that the device discriminates hemoglobin levels with high fidelity.

Quantitatively (Table 4.7), the proposed sensor achieves a nearly constant S of $\sim$ 476nm/RIU for Cells B–E, which is $\approx$ 45–59% higher than Saini and Awasthi's 300–328nm/RIU. The measured line width remains narrow (FWHM = 0.02–0.03 nm), yielding $Q \approx (25.7 \times 10^3)$–$(39.2 \times 10^3)$. Compared with [76], our Q is higher at one operating point (Cell B) but lower for Cells C–E, primarily because [76] reports ultra-narrow line widths ($\sim$ 0.010 nm) in those cases.

The FoM reflects this trade-off: our design attains a substantially larger FoM at Cell

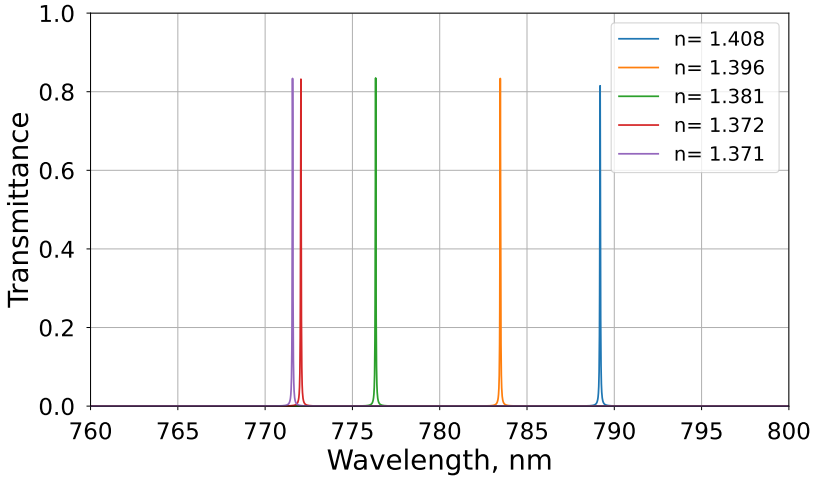

Figure 4.4: Transmittance spectra of the 1D PhC sensor for varying hemoglobin concentration (C_HB) in red blood cells

Table 4.7: Comparison of S, Q, peak wavelength $\lambda_{\max}$ and FWHM of the proposed 1D PhC sensor, compared with Saini and Awasthi [76].

Hemoglobin concentration C_{HB}	**Cell A** 30.900 g/dL	**Cell B** 25.599 g/dL	**Cell C** 19.789 g/dL	**Cell D** 16.289 g/dL	**Cell E** 15.990 g/dL
$\lambda_{\max}$ (Saini et al. [76])	671.40	667.80	662.70	659.60	659.20
$\lambda_{\max}$ (our work)	789.19	783.47	776.33	772.05	771.57
FWHM (Saini et al. [76])	0.11	0.036	0.0135	0.010	0.0095
FWHM (our work)	0.03	0.02	0.03	0.03	0.03
S (Saini et al. [76])	–	300.00	322.20	327.70	310.50
S (current work)	–	476.67	476.30	476.11	476.22
Q (Saini et al. [76])	6,103.63	18,550.00	49,088.80	65,960.00	69,389.47
Q (our work)	26,306.33	39,173.50	25,877.67	25,735.00	25,719.00
FoM (Saini et al. [76])	–	8,333.3	23,866.7	32,770	32,684.2
FoM (our work)	–	23,833.33	15,876.54	15,870.37	15,873.87

B (23,833 vs. 8,333) but lower FoM for Cells C–E due to their comparatively broader FWHM. Overall, the consistent red shift with increasing C_{HB}, the high S, and kHz-level spectral selectivity (via large Q) indicate that the 1D PhC sensor can reliably resolve clinically relevant changes in hemoglobin. Further narrowing of the resonance (e.g., via impedance matching or defect-mode tailoring) should raise Q and FoM without sacrificing the observed S.

4.5 Conclusion

This chapter presented the simulation results and analysis of the proposed photonic crystal biosensor. The main findings can be summarized as follows:

- The biosensor demonstrates high S to refractive index variations of blood components.

- The optimized configuration ($N = 7$, $d_0 = 10D$, $\theta = 20^\circ$) provides sharp resonance peaks with a high Q.
- The sensor successfully detects variations in hemoglobin concentration and shows potential for clinical applications such as malaria detection and anemia diagnosis.

Overall, the study confirms that 1D PhCs with defect cavities are powerful platforms for biosensing, combining high performance with practical applicability in biomedical diagnostics.

General Conclusion

This dissertation set out to design, model, and experimentally motivate a one-dimensional photonic crystal (1D PhC) platform for RI biosensing. By combining dispersion-aware multilayer synthesis with physics-grounded analysis, we translated conceptual band-gap control into manufacturable stacks and defect-cavity resonators that deliver sharp spectral signatures under realistic operating conditions.

We developed a rigorous yet efficient modeling pipeline based on the Transfer Matrix Method (TMM), anchored in Maxwell's boundary conditions and validated against complementary viewpoints (mode and time-domain reasoning). Material dispersion for SiO_2/TiO_2 guided quarter-wave designs around a target wavelength, while parametric sweeps quantified sensitivity (S), quality factor (Q), signal-to-noise ratio (SNR), and figure of merit (FOM). Throughout, we emphasized robustness to fabrication tolerances and angular/polarization dependencies that often degrade ideal performance.

Summary of principal findings.

- We established a compact TMM workflow that reliably predicts multilayer spectra for TE/TM polarizations and oblique incidence, enabling rapid exploration of design spaces at negligible computational cost.
- Quarter-wave SiO_2/TiO_2 Bragg mirrors provide wide stopbands; inserting a single defect layer yields high-contrast, narrow resonances with controllable linewidth via index contrast, bilayer count, and defect thickness.
- Sensitivity and selectivity trade off with insertion loss and spectral crowding: increasing period number reduces leakage and narrows resonances, but can introduce multiple nearby modes; optimum regimes were identified that jointly maximize S, Q, and FOM.
- Angular interrogation offers tunable resonance shifts without sacrificing robustness when the design targets a moderate incident angle; polarization splitting can be minimized by balanced optical thicknesses.
- Tolerance studies indicate that RI and thickness errors have asymmetric effects on resonance position and Q; dispersion-aware targets mitigate drift, and modest post-fabrication angle trimming recovers design points.

- Using hemoglobin as a representative analyte, the optimized cavity demonstrates RI detection with competitive S and FOM compared to literature baselines while retaining fabrication simplicity and CMOS compatibility.

Significance. The thesis contributes a design methodology that is both physically interpretable and fabrication-conscious, clarifying how material choice, optical thickness, and cavity engineering interact to produce usable biosensing windows. The resulting guidelines are portable to alternative material systems and readout schemes.

Perspectives and future work.

- *Dual-cavity and Vernier schemes:* cascade two defect cavities to enhance discrimination and extend the unambiguous index range.
- *Impedance-matched terminations:* use gradient or apodized layers to suppress sidelobes and improve insertion loss without sacrificing Q.
- *Multi-parameter sensing:* co-design polarization/angle readouts to decouple temperature drift from RI changes.
- *Functionalization and microfluidics:* integrate selective surface chemistry and compact flow cells to elevate specificity and sample throughput.
- *Data-driven calibration:* apply spectral fitting and lightweight learning-based regressors for real-time, tolerance-aware inference.
- *Materials and band tailoring:* explore high-index-contrast dielectrics and hybrid stacks (e.g., Si_3N_4, Ta_2O_5) to push stopband width and reduce absorption at the target wavelength.

In closing, this work demonstrates that carefully engineered 1D PhC defect structures can provide sensitive and stable biosensing performance for human blood component detection. The presented numerical study based on the Transfer Matrix Method (TMM) confirms the effectiveness of the proposed SiO_2/TiO_2 structure and highlights the influence of structural parameters on sensor behavior, providing a useful foundation for future biomedical sensing investigations and related optical sensing applications.

References

[1] Dennis W Prather, Shouyuan Shi, Janusz Murakowski, Garrett J Schneider, Ahmed Sharkawy, Caihua Chen, and Binglin Miao. "Photonic crystal structures and applications: Perspective, overview, and development". *IEEE Journal of Selected Topics in Quantum Electronics* 12.6 (2007), pp. 1416–1437.

[2] Maksim Skorobogatiy and Jianke Yang. *Fundamentals of photonic crystal guiding*. Cambridge university press, 2009.

[3] Dennis W Prather, Ahmed S Sharkawy, Shouyuan Shi, and Mathew J Zablocki. "Design and applications of photonic crystals". *Handbook of Nanoscience, Engineering, and Technology*. CRC Press, 2018, pp. 492–535.

[4] Amit Kumar Goyal and Ajay Kumar. "Recent Advances and Trends in Photonic Crystal Technology" (2024).

[5] MA Butt, Svetlana Nikolaevna Khonina, and NL Kazanskiy. "Recent advances in photonic crystal optical devices: A review". *Optics & Laser Technology* 142 (2021), p. 107265.

[6] Andrea Blanco and Joseba Zubía. "Photonic Band Gap Engineered Materials for Controlling the Group Velocity of Light". *Advanced Photonic Sciences*. IntechOpen, 2012.

[7] Arafa H Aly. "Electromagnetic waves propagation characteristics in superconducting photonic crystals". Sciyo Rijeka, 2011, pp. 75–82.

[8] M Clara and Amadeu Griol. "Photonic Bandgap Glass-Based Structures". *Overall Aspects of Non-Traditional Glasses: Synthesis, Properties and Applications*. Bentham Science Publishers, 2016, pp. 107–130.

[9] Kazuaki Sakoda and Joseph W Haus. "Science and engineering of photonic crystals". *Progress in optics*. Vol. 54. Elsevier, 2010, pp. 271–317.

[10] Susumu Noda and Toshihiko Baba. "Physical and experimental background of photonic crystals". *Roadmap on Photonic Crystals*. Springer, 2003, pp. 1–11.

[11] Philip Russell. "Photonic crystal fibers: a historical account". *IEEE Leos Newsletter* 21.5 (2007), pp. 11–15.

[12] Costas M Soukoulis. “Back to basics: history of photonic crystals and metamaterials”. *Photoniques* (2018), pp. 50–56.

[13] P. C. Hoang. “Applications of Photonic Crystals in Communications Engineering and Optical Imaging”. PhD thesis. Technische Universitat Kaiserslautern, 2009.

[14] A. S. Firouzjaei, S. S. Afghahi, and A. A. E. Valmoozi. “Emerging Trends, Applications, and Fabrication Techniques in Photonic Crystal Technology”. *Recent Advances and Trends in Photonic Crystal Technology*. IntechOpen, 2024.

[15] G. Miriyala, V. K. Velpula, S. Yechuri, B. Sridhar, and G. V. Vinod. “A Survey on Photonics and its Applications”. *Journal of Physics: Conference Series*. Vol. 2837. 1. IOP Publishing. 2024, p. 012041.

[16] M. Kolle. “Static and Tuneable One-Dimensional Photonic Structures”. *Photonic Structures Inspired by Nature*. Berlin, Heidelberg: Springer Berlin Heidelberg, 2011, pp. 79–98.

[17] D. Kou, S. Zhang, and W. Ma. “Recent advances in 1D photonic crystals: diverse morphologies and distinctive structural colors for multifaceted applications”. *Advanced Optical Materials* 12.19 (2024), p. 2400192.

[18] M. Roussey, E. Descrovi, M. Hayrinen, A. Angelini, M. Kuittinen, and S. Honkanen. “One-dimensional photonic crystals with cylindrical geometry”. *Optics Express* 22.22 (2014), pp. 27236–27241.

[19] T. Q. Zhu, Y. M. Liu, J. T. Zhang, and H. F. Zhang. “The Absorption Properties of One-Dimensional Spherical Photonic Crystals Based on Magnetized Ferrite Materials”. *Annalen der Physik* 535.2 (2023), p. 2200370.

[20] V. A. Ilinykh and L. B. Matyushkin. “Fabrication of one-dimensional photonic crystals by sol-gel method”. *2016 IEEE NW Russia Young Researchers in Electrical and Electronic Engineering Conference (EIConRusNW)*. 2016, pp. 47–50.

[21] R. M. Almeida, R. E. Rojas-Hernandez, and L. F. Santos. “One-dimensional multilayer photonic crystals”. *Sol-Gel Derived Opt Photonic Mater*. 2020, pp. 75–94.

[22] V. P. Stinson, S. Park, M. McLamb, G. Boreman, and T. Hofmann. “One-Dimensional Photonic Crystals with Narrow-Band Defect Modes Fabricated by Direct Laser Writing”. *2022 IEEE Research and Applications of Photonics in Defense Conference (RAPID)*. 2022, pp. 1–2.

[23] R. A. Wahsheh, Z. Lu, and M. A. Abushagur. “Crosstalk reduction in square cavities”. *IEEE Photonics Journal* 1.3 (2009), pp. 191–196.

[24] M. Qiu and S. He. “Large complete band gap in two-dimensional photonic crystals with elliptic air holes”. *Physical Review B* 60.15 (1999), p. 10610.

[25] A. Zarei and M. Shahabadi. “Design of photonic crystal fibers with desired dispersion properties”. *Optics Communications* 281.17 (2008), pp. 4479–4484.

[26] S. G. Johnson, S. Fan, P. R. Villeneuve, J. D. Joannopoulos, and L. A. Kolodziejski. “Guided modes in photonic crystal slabs”. *Physical Review B* 60.8 (1999), p. 5751.

[27] L. Pang, W. Nakagawa, and Y. Fainman. “Fabrication of two-dimensional photonic crystals with controlled defects by use of multiple exposures and direct write”. *Applied Optics* 42.27 (2003), pp. 5450–5456.

[28] A. Djoudi, L. Legouezigou, S. Hubert, S. Sainson, C. Moussant, J. P. Chandouineau, and G. H. Duan. “Fabrication of two-dimensional InP photonic bandgap structures using inductively coupled plasma etching”. *Conference Proceedings. 14th Indium Phosphide and Related Materials Conference*. 2002, pp. 429–432.

[29] S. Shoji, H. B. Sun, and S. Kawata. “Photofabrication of wood-pile three-dimensional photonic crystals using four-beam laser interference”. *Applied physics letters* 83.4 (2003), pp. 608–610.

[30] V. Piccolo, A. Chiappini, A. Vaccari, A. C. Lesina, M. Ferrari, L. Deseri, and D. Zonta. “Validating 3D photonic crystals for structural health monitoring”. *Structural Health Monitoring 2017*. 2017.

[31] R. Hillebrand and W. Hergert. “Scaling properties of a tetragonal photonic crystal design having a large complete bandgap”. *Photonics and Nanostructures-Fundamentals and Applications* 2.1 (2004), pp. 33–39.

[32] D. C. Meisel, M. Deubel, M. Hermatschweiler, K. Busch, W. Koch, G. von Freymann, and M. Wegener. “Three-dimensional photonic crystals”. *Solid State Phenomena* 99 (2004), pp. 55–64.

[33] A. Numata and K. Nobayashi. “U.S. Patent No. 7,697,810”. (Washington, DC). 2010.

[34] S. M. Yang and G. R. Lee. “Three-dimensional (3D) photonic bandgap crystals: fabrication and applications”. *Korean Chemical Engineering Research* 41.3 (2003), pp. 36–277.

[35] S. Wang, K. Tamamori, T. Motoi, M. Okunuki, H. Ono, and T. Aiba. “U.S. Patent No. 7,700,390”. (Washington, DC). 2010.

[36] P. S. J. Russell. “Photonic band gaps”. *Physics world* 5.8 (1992), p. 37.

[37] J. Singh. *Electronic and optoelectronic properties of semiconductor structures*. Cambridge University Press, 2007.

[38] J. Singleton. *Band theory and electronic properties of solids*. Vol. 2. OUP Oxford, 2001.

[39] P. Contu. *Band structure in photonic crystals analytical and numerical methods.* 2011.

[40] R. M. De La Rue and S. A. De La Rue. "Introduction to photonic crystals and photonic band-gaps". *Photonic Crystals: Physics and Technology.* Milano: Springer Milan, 2008, pp. 7–25.

[41] K. M. Ho, C. T. Chan, and C. M. Soukoulis. "Photonic gaps for electromagnetic waves in periodic dielectric structures: Discovery of the diamond structure". *Photonic band gaps and localization.* Boston, MA: Springer US, 1993, pp. 235–245.

[42] F. L. Qi, Q. Li, C. F. Ding, and J. B. Wu. "Fabrication strategies and microscale sensing functionalities of mechanochromic colloidal photonic crystals for underwater applications". *Microstructures* 5.1 (2025), N–A.

[43] D. N. Chigrin and C. M. Sotomayor Torres. "Periodic thin-film interference filters as one-dimensional photonic crystals". *Optics and Spectroscopy* 91.3 (2001), pp. 484–489.

[44] R. Paschotta. "Bragg mirrors". *Encyclopedia of Laser Physics and Technology* (2009).

[45] Y. Fan, Z. Wei, H. Li, H. Chen, and C. M. Soukoulis. "Photonic band gap of a graphene-embedded quarter-wave stack". *Physical Review B–Condensed Matter and Materials Physics* 88.24 (2013), p. 241403.

[46] F. Intonti, S. Vignolini, M. Colocci, and D. S. Wiersma. "PHOTONIC CRYSTALS: Photons flow in liquid circuits". *Laser Focus World* 1 (2007), pp. 72–73.

[47] P. Kuchment. "The mathematics of photonic crystals". *Mathematical modeling in optical science.* Society for Industrial and Applied Mathematics, 2001, pp. 207–272.

[48] H. H. C. Kang. *Fabrication of ceramic layer-by-layer infrared wavelength photonic band gap crystals.* Tech. rep. IS-T 2082. Ames Lab., Ames, IA (United States), 2004.

[49] F. Segovia-Chaves, H. Vinck-Posada, V. Dhasarathan, and M. M. Rajan. "Transmittance spectrum in a 1D photonic crystal composed fused silica and sea water". *Optik* 185 (2019), pp. 930–935.

[50] S. P. Palto, Y. A. Draginda, V. V. Lazarev, and S. G. Yudin. "Electrooptic properties of one-dimensional photonic crystals based on organic ferroelectric and dye". *Journal of Experimental and Theoretical Physics* 119.3 (2014), pp. 384–391.

[51] J. V. Malik, K. D. Jindal, V. Kumar, V. Kumar, A. Kumar, K. S. Singh, and T. P. Singh. "Effect of Temperature on Photonic Band Gaps in Semiconductor-Based One-Dimensional Photonic Crystal". *Advances in Optical Technologies* 2013.1 (2013), p. 798087.

[52] A. Sanchez and S. Orozco. "Elasto-optical effect on the band structure of a one-dimensional photonic crystal under hydrostatic pressure". *Journal of the Optical Society of America B* 33.7 (2016), pp. 1406–1410.

[53] B. Belyaev, V. Tyurnev, and V. Shabanov. "One-dimensional photonic crystal bandpass filters". *Doklady Physics*. Vol. 59. 2. 2014.

[54] A. Haryanto, Y. J. Eo, Y. R. Do, and C. W. Lee. "Layer-by-layer assembly of 1-D photonic crystal for wavelength-selective optical filter". *Applied Surface Science* 611 (2023), p. 155762.

[55] M. Mansuripur. "Omni-directional dielectric mirrors". *Opt. Photon. News* 9 (2001), pp. 46–50.

[56] I. E. Shaaban, A. S. Samra, S. Muhammad, and S. Wageh. "Design of Distributed Bragg Reflectors for Green Light-Emitting Devices Based on Quantum Dots as Emission Layer". *Energies* 15.3 (2022), p. 1237.

[57] A. Panda and P. D. Pukhrambam. "Design and analysis of one-dimensional photonic crystal biosensor device for identification of cancerous cells". *Next Generation Smart Nano-Bio-Devices*. Singapore: Springer Nature Singapore, 2022, pp. 153–169.

[58] M. Medhat, C. Malek, M. Tilja, M. R. Abukhadra, S. Bellucci, H. A. Elsayed, and A. Mehaney. "One-dimensional photonic crystals comprising two different types of metamaterials for the simple detection of fat concentrations in milk samples". *Nanomaterials* 14.21 (2024), p. 1734.

[59] G. Morthier and P. Vankwikelberge. *Handbook of distributed feedback laser diodes*. Artech House, 2013.

[60] P. O. Leisher, J. D. Sulkin, and K. D. Choquette. "Parametric study of proton-implanted photonic crystal vertical-cavity surface-emitting lasers". *IEEE Journal of Selected Topics in Quantum Electronics* 13.5 (2007), pp. 1290–1294.

[61] I. Celanovic, F. O'Sullivan, N. Jovanovic, M. Qi, and J. G. Kassakian. "1D and 2D photonic crystals for thermophotovoltaic applications". *Photonic Crystal Materials and Nanostructures*. Vol. 5450. SPIE. 2004, pp. 416–422.

[62] C. L. M. Hofmann, S. Fischer, E. H. Eriksen, et al. "Experimental validation of a modeling framework for upconversion enhancement in 1D-photonic crystals". *Nature Communications* 12.1 (2021), p. 104.

[63] H. J. Joo, Y. Kim, D. Burt, Y. Jung, L. Zhang, M. Chen, and D. Nam. "1D photonic crystal GeSn-on-insulator nanobeam laser". *Silicon Photonics XVII*. Vol. 12006. SPIE. 2022, pp. 142–150.

[64] R. Osgood Jr and X. Meng. *Principles of photonic integrated circuits*. 2021.

[65] Y. Lu, H. Xia, G. Zhang, and C. Wu. "Electrically tunable block copolymer photonic crystals with a full color display". *Journal of Materials Chemistry* 19.33 (2009), pp. 5952–5955.

[66] Luca Nucara, Francesco Greco, and Virgilio Mattoli. "Electrically responsive photonic crystals: a review". *Journal of Materials Chemistry C* 3.33 (2015), pp. 8449–8467.

[67] A. Bahtiar and I. A. Dharmawan. "Nonlinear Photonic Crystal for All-optical Switching Appli". *Bionatura* 9.3 (2007).

[68] S. Tavana, S. Bahadori-Haghighi, and M. H. Sheikhi. "High-performance electro-optical switch using an anisotropic graphene-based one-dimensional photonic crystal". *Optics Express* 30.6 (2022), pp. 9269–9283.

[69] Hiroyuki Fujiwara. *Spectroscopic Ellipsometry: Principles and Applications*. Chichester, UK: John Wiley & Sons, 2007. ISBN: 9780470016084. DOI: 10.1002/9780470060193.

[70] Pochi Yeh and Michael Hendry. *Optical waves in layered media*. 1990.

[71] Kane Yee. "Numerical solution of initial boundary value problems involving maxwell's equations in isotropic media". *IEEE Transactions on Antennas and Propagation* 14.3 (1966), pp. 302–307. DOI: 10.1109/TAP.1966.1138693.

[72] Min Qiu. "Computational methods for the analysis and design of photonic bandgap structures". PhD thesis. KTH, 2000.

[73] MAACHE Mouhssin. "Design and Optical Studies of Photonic Components Using Slow Light Properties «Conception et Etudes Optiques de Composants Photoniques en Utilisant Les Propriétés de Lumière Lente»". PhD thesis. MINISTRY OF HIGHER EDUCATION, 2019.

[74] Sanshui Xiao, Linfang Shen, and Sailing He. "A plane-wave expansion method based on the effective medium theory for calculating the band structure of a two-dimensional photonic crystal". *Physics Letters A* 313.1-2 (2003), pp. 132–138.

[75] Young-Chung Hsue, Arthur J Freeman, and Ben-Yuan Gu. "Extended plane-wave expansion method in three-dimensional anisotropic photonic crystals". *Physical Review B—Condensed Matter and Materials Physics* 72.19 (2005), p. 195118.

[76] Sujit Kumar Saini and Suneet Kumar Awasthi. “Sensing and detection capabilities of one-dimensional defective photonic crystal suitable for malaria infection diagnosis from preliminary to advanced stage: theoretical study”. *Crystals* 13.1 (2023), p. 128.

[77] Abinash Panda and Puspa Devi Pukhrambam. “Investigation of defect based 1D photonic crystal structure for real-time detection of waterborne bacteria”. *Physica B: Condensed Matter* 607 (2021), p. 412854.

[78] Mikhail N Polyanskiy. “Refractiveindex. info database of optical constants”. *Scientific Data* 11.1 (2024), p. 94.

[79] Vijay Shanker Chaudhary, Dharmendra Kumar, Bramha P Pandey, and Santosh Kumar. “Advances in photonic crystal fiber-based sensor for detection of physical and biochemical parameters—A review”. *IEEE sensors journal* 23.2 (2022), pp. 1012–1023.

[80] Sanjeev K Srivastava. “design of temperature sensor based on one-dimensional photonic crystal containing Si–BGO layer”. *Materials Open* 1 (2023), p. 2350003.

[81] Ayman A Ameen, Abinash Panda, Ahmed Mehaney, Abdulkarem HM Almawgani, Dipika D Pradhan, Ghassan Ahmed Ali, Yahya Ali Abdelrahman Ali, and Hussein A Elsayed. “An investigation of high-performance pressure sensor employing a polymer-defect-based 1D annular photonic crystal”. *Photonics*. Vol. 10. 7. MDPI. 2023, p. 731.

[82] Alexander Poletaev. “Composition of the blood and reflection of the health state of human body”. *Biomedical and Pharmacology Journal* 11.4 (2018), pp. 1797–1800.

[83] James T Yurkovich and Leroy Hood. “Blood is a window into health and disease”. *Clinical chemistry* 65.10 (2019), pp. 1204–1206.

[84] Barbara J Bain. “Structure and function of red and white blood cells and platelets”. *Medicine* 49.4 (2021), pp. 183–188.

[85] Eleanor Humphry and Catherine E Armstrong. “Physiology of red and white blood cells”. *Anaesthesia & Intensive Care Medicine* 23.2 (2022), pp. 118–122.

[86] Martin J Page and Etheresia Pretorius. “Platelet behavior contributes to neuropathologies: a focus on Alzheimer’s and Parkinson’s disease”. *Seminars in Thrombosis and Hemostasis*. Vol. 48. 03. Thieme Medical Publishers, Inc. 2022, pp. 382–404.

[87] PD Sturkie and P Griminger. “Blood: physical characteristics, formed elements, hemoglobin, and coagulation”. *Avian physiology*. Springer, 1976, pp. 53–75.

[88] AB Poletaev, AI Trukhanov, and AV Grechko. "MOLECULAR COMPOSITION OF BLOOD PLASMA AND CONDITION OF HUMAN ORGANISM AT THE NORMAL AND PATHOLOGICAL STATE". *Physical and rehabilitation medicine, medical rehabilitation* 1.2 (2019), pp. 37–42.

[89] Nazmi A Mohammed, Mahmoud M Hamed, Ashraf AM Khalaf, Abdulaziz Alsayyari, and S El-Rabaie. "High-sensitivity ultra-quality factor and remarkable compact blood components biomedical sensor based on nanocavity coupled photonic crystal". *Results in Physics* 14 (2019), p. 102478.

[90] Ekaterina N Lazareva and Valery V Tuchin. "Blood refractive index modelling in the visible and near infrared spectral regions". *Journal of biomedical photonics & engineering* 4.1 (2018), pp. 35–41.

[91] Arafa H Aly, Zaky A Zaky, Ahmed S Shalaby, Ashour M Ahmed, and D Vigneswaran. "Theoretical study of hybrid multifunctional one-dimensional photonic crystal as a flexible blood sugar sensor". *Physica Scripta* 95.3 (2020), p. 035510.

[92] Arafa H Aly, Hussein A Elsayed, and Christina Malek. "Optical properties of one-dimensional defective photonic crystal containing nanocomposite material". *Journal of Nonlinear Optical Physics & Materials* 26.01 (2017), p. 1750007.

[93] Omar A Abd El-Aziz, Hussein A Elsayed, and Marwa I Sayed. "One-dimensional defective photonic crystals for the sensing and detection of protein". *Applied Optics* 58.30 (2019), pp. 8309–8315.

[94] Zaky A Zaky, Ashour M Ahmed, Ahmed S Shalaby, and Arafa H Aly. "Refractive index gas sensor based on the Tamm state in a one-dimensional photonic crystal: Theoretical optimisation". *Scientific reports* 10.1 (2020), p. 9736.